Manipulating Spin-Lattice Coupling in Layered Magnetic Topological Insulator Heterostructure *via* Interface Engineering

Sujan Maity,[1] Dibyendu Dey,[2] Anudeepa Ghosh,[1] Suvadip Masanta,[3] Binoy Krishna De,[4] Hemant Singh Kunwar,[4] Bikash Das,[1] Tanima Kundu,[1] Mainak Palit,[1] Satyabrata Bera,[1] Kapildeb Dolui,[5] Kenji Watanabe,[6] Takashi Taniguchi,[7] Liping Yu,[2] A Taraphder,[8] and Subhadeep Datta*[1]

[1]*School of Physical Sciences, Indian Association for the Cultivation of Science, 2A & 2B Raja S. C. Mullick Road, Jadavpur, Kolkata - 700032, India*

[2]*Department of Physics and Astronomy, University of Maine, Orono, ME 04469, USA*

[3]*Bose Institute, Department of Physics Main Campus 93/1, A. P. C. Road Kolkata - 700 009, India*

[4]*UGC-DAE Consortium for Scientific Research, Indore Centre, University Campus, Khandwa Road, Indore 452001*

[5]*Lomare Technolgies Limited, 6 London Street, London EC3R 7LP, United Kingdom*

[6]*Research Center for Functional Materials, National Institute for Materials Science, Tsukuba 305-0044, Japan*

[7]*International Center for Materials Nanoarchitectonics, National Institute for Materials Science,Tsukuba 305-0044, Japan*

[8]*Department of Physics, Indian Institute of Technology Kharagpur, W.B. 721302, India*

Abstract

Induced magnetic order in a topological insulator (TI) can be realized either by depositing magnetic adatoms on the surface of a TI or engineering the interface with epitaxial thin film or stacked assembly of two-dimensional (2D) van der Waals (vdW) materials. Herein, we report the observation of spin-phonon coupling in the otherwise non-magnetic TI Bi_2Te_3, due to the proximity of $FePS_3$ (an antiferromagnet (AFM), $T_N \sim 120$ K), in a vdW heterostructure framework. Temperature-dependent Raman spectroscopic studies reveal deviation from the usual phonon anharmonicity originated from spin-lattice coupling at the $Bi_2Te_3/FePS_3$ interface at/below 60 K in the peak position (self-energy) and linewidth (lifetime) of the characteristic phonon modes of Bi_2Te_3 (106 cm^{-1} and 138 cm^{-1}) in the stacked heterostructure. The Ginzburg-Landau (GL) formalism, where the respective phonon frequencies of Bi_2Te_3 couple to phonons of similar frequencies of $FePS_3$ in the AFM phase, has been adopted to understand the origin of the hybrid magneto-elastic modes. At the same time, the reduction of characteristic T_N of $FePS_3$ from 120 K in isolated flakes to 65 K in the heterostructure, possibly due to the interfacial strain, which leads to smaller Fe-S-Fe bond angles as corroborated by computational studies using density functional theory (DFT). Besides, inserting hexagonal boron nitride within $Bi_2Te_3/FePS_3$ stacking regains the anharmonicity in Bi_2Te_3. Controlling interfacial spin-phonon coupling in stacked heterostructure can have potential application in surface code spin logic devices.

INTRODUCTION

The realization of the quantum anomalous Hall effect (QAHE) and topological magneto-electric effect (TMAE) depends on the functional electronic interface between the (anti-)ferromagnet and topological insulator (TI) in the engineered heterostructure framework. Effect on Dirac cone-like surface state of TI due to hybridization and charge transfer across the interface and subsequent formation of an exchange gap due to proximity effects result in an efficient control over the exotic state [1]. Recently, a series of experiments on TIs doped with 3d transition metals [2–5] has lead to the observation of broken time-reversal symmetry (TRS) and the consequent opening of a band gap in the surface band structure. Moreover, magnetically doped-TI shows current-induced giant spin-orbit torque (SOT) which in turn may result in ultra-low power memory and logic devices [6]. But still, the sample inhomogeneity and the formation of a disordered cluster in ferromag-

netically doped TIs, even with ppm level of doping concentration, restricts the anomalous Hall regime to one or two orders of magnitude less than the Curie-temperature ($T_C \sim 30$ K for magnetically doped Bi-Sb alloy) [7]. However, in the interface-controlled magnetic heterostructure (*e.g.* Fe overlayer is deposited on TI), one may preserve long-range ferromagnetism at ambient temperature [8]. Even so, in this metallic FM-TI heterostructure, the possibility of alteration of the topological surface state due to intermixing with the bulk charge carriers, and most importantly, metallic iron film working as a short circuit on TI would impede future spintronic device applications. Furthermore, epitaxial integration (molecular beam epitaxy) of a high-quality thin film of topological insulator (*e.g.* Bi_2Te_3, Bi_2Se_3) on insulating magnetic substrate (*e.g.* $Y_3Fe_5O_{12}$, EuS), with slightest chemical reaction at the interface, can show AHE but limited to low temperature ($\sim$22 K for EuS) due to the choice of the magnet [9]. Even for antiferromagnets (AFM) exhibiting no macroscopic magnetization, while short-range interfacial exchange coupling [10] in the interface can be crucial for manipulating magnetic state, as reported in CrSb (AFM with $T_N \sim$ 700 K)/Cr-doped(Bi, Sb)$_2$Te$_3$ (FM with $T_C \sim 35$ K) thin film superlattice [11], doping and heterostructure engineering checks the temperature scale close to 50 K. Also, the high sensitivity of the surface states of TI to air exposure puts a limit on the sample characterization and applicability.

For an atomically-flat interface with reasonable air-stability (see Supplementary Information Fig. S19), layered two-dimensional (2D) material-based van der Waals heterostructures (vdWh) are proving to be better to create proximity-induced effects in low-power electronic circuits [12]. For example, introducing graphene (Graphene / Europium oxide (EuO) [13], Graphene/$BiFeO_3$ [14], Graphene/EuS[15], Graphene/yttrium-iron-garnet (YIG) [16]) with magnetic thin films may be used as an electrical read-out of the magnetic order. Moreover, modulation of interfacial spin texture and long-range exchange coupling mediated by magnetic order significantly enhances the transition temperature in the superlattice [13]. In fact, the net magnetic moment induced on graphene due to magnetic proximity (0.1 μ_B per C atom) is nearly double that of Pt on magnetic insulator (MI), as reported in the x-ray magnetic circular dichroism (XMCD) studies [17]. In the case of vdW semiconductor-magnet heterostructure, or in other words, valley-spin related device consisting of layered transition metal dichalcogenide (TMDC), theoretical predictions have been made where an induced Zeeman field creates giant valley splitting ($\sim$ 300 meV) due to proximity effect in case of (i) ferromagnetic heterostructure in $MoTe_2$-EuO [18], and (ii) antiferromagnets as in WS_2-MnO(111) [19], MoS_2-CoO(111) [20] and TMD-CrI_3 [21]. As furtherance, the stacked all-2D assembly offers proximity-induced spin-texture with controlled magnetic anisotropy to-

gether with persistent magnetoresistance above transition temperature which has been reported in graphene - vdW FM ($Cr_2Ge_2Te_6$ with $T_C \sim 60$ K) heterostructure [22].

TI-MI heterostructures with vdW materials have been intensively studied using electronic transport measurements of micro/nano-electronic devices fabricated *via* lithography [23]. But, probing the contributions of each constituent layer in the stacking is difficult to conclude from conventional magnetoresistance measurements. Alternatively, Raman spectroscopy offers an indirect tool to detect characteristic phonon mode/s, elementary excitations (*e.g.* magnons), spin-phonon and electron-phonon coupling in 2D magnets (for example, in ferromagnets Fe_3GeTe_2 [24], $CrSiTe_3$ [25], and in antiferromagnets $FePS_3$ [26]) and topological insulators (Bi_2Te_3 [27], Bi_2Se_3 [28]) in its few-atomic layer form. In particular, magnetic transition in *strictly-2D* magnets with magnetic anisotropy can easily be detected *via* spin-phonon coupling, as analyzed by Ghosh *et al.*[26] in case of $FePS_3$ by marking the point of deviation (hardening or softening of phonon modes) in temperature-dependent phonon anharmonicity. Note that out of all predicted and experimentally verified 2D FMs and AFMs, $FePS_3$, an antiferromagnet ($T_N \sim 120$ K in bulk), shows layer-thickness independent transition temperature [26, 29] which could be crucial for high-temperature applications keeping 2D nature of the heterostructure intact. Also, the pristine quality of less-strained micromanipulated structure with TI which provides low density of states (DOS) at the interface and the greater probability of hybridization with the electronic states from the overlying layered magnets, creates an ideal platform to study the material-specific modification *via* recognizing the Raman modes as a function of temperature. To the best of our knowledge, there are no reports to date that concerns Raman spectroscopic studies on proximity-induced magnetic order on TI in engineered vdW AFM-TI heterostructure.

Here, we present temperature-dependent Raman spectroscopic studies on *all-2D* topological insulator (Bi_2Te_3) - antiferromagnet ($FePS_3$) vdW heterostructure stacked on Si/SiO_2 substrate. With temperature (down to 5 K), we track all the characteristic phonon modes of (i) $FePS_3$ which have previously been observed to demonstrate spin-phonon coupling (250 cm^{-1}, 280 cm^{-1} and 380 cm^{-1}), zone-folding (around 105 cm^{-1}), and magnon (120 cm^{-1}), and (ii) Bi_2Te_3 (106 cm^{-1} and 138 cm^{-1}), and analyze the data with the anharmonic phonon-decay model. We note that observed deviation from the usual phonon anharmonicity in peak position (self-energy) and linewidth (lifetime) of the mentioned Raman modes of Bi_2Te_3 in the heterostructure ($T^* \sim 60$ K) indicates spin-phonon coupling which is, otherwise, not present in an isolated flake. Bi_2Te_3 recover its anharmonicity in heterostructure when hexagonal boron nitride (hBN) is placed in between Bi_2Te_3

and $FePS_3$. Also, the characteristic antiferromagnetic Néel temperature (T_N) of $FePS_3$ reduces from 120 K (in isolated flake) to 65 K, in the heterostructure possibly due to the interfacial strain which leads to smaller Fe-S-Fe bond angles without varying magnetic anisotropic energy (MAE) which has been investigated using density functional theory (DFT) calculations. Spatial control of magnetic proximity-induced spin-phonon coupling in layered stacking of magnetic topological insulator may open up novel pathways for future gate-tunable all-2D spintronic logic devices.

EXPERIMENTAL DETAILS

Binary Bi_2Te_3 single crystal was grown through the solid-state reaction method by using box furnace (see the method section for growth details) [30]. Single crystal $FePS_3$ was grown by the chemical vapor transport (CVT) method in two zone tube furnace as reported in [31]. Bi_2Te_3 crystal was micromechanically exfoliated by standard scotch tape and transferred onto 300 nm Si/SiO_2 substrate by dry transfer method [32]. Suitable flake was located by using Optical Microscope (OLYMPUS BX53M)) by comparing transparency of the flake. Heterostructures consist of Bi_2Te_3, $FePS_3$ and hBN are fabricated by placing one material onto another by using micromanipulator. The fabricated heterostructures (HS) are: (a) HS-1: Bulk Bi_2Te_3 (>500 nm)/ Bulk $FePS_3$($\sim$150 nm); (b) HS-2: Bulk Bi_2Te_3 ($\sim$ 250 nm)/Bulk $FePS_3$($\sim$ 88 nm); (c) HS-3: Bulk Bi_2Te_3 ($\sim$140 nm)/ few layer $FePS_3$($\sim$10 nm) and (d) HS-4: Bulk Bi_2Te_3 (>500 nm) /Bulk hBN(>100 nm)/Bulk $FePS_3$ ($\sim$ 150 nm) and (e) HS-5: Bulk Bi_2Te_3 (>500 nm) /few layer hBN($\sim$10 nm)/Bulk $FePS_3$ ($\sim$ 150 nm) . Room temperature and temperature-dependent Raman measurements of isolated Bi_2Te_3, and these heterostructures were carried out by using Jobin Yvon Horibra LABRAM-HR 800 visible micro Raman system and a 473 nm wavelength radiation from a diode laser as an excitation source. All measurements were performed under high vacuum (10^{-6} mbar) using a liquid helium cryostat (Janis ST-500). Laser beam was focused through a microscope objective with 50x magnification and a spot size of 1μm. Laser power was kept below 200μW to avoid sample heating.

RESULTS

The crystal structure of Bi_2Te_3 contains covalently bonded five mono-atomic planes, which form a quintuple layer (Te-Bi-Te-Bi-Te), weakly bound by van der Waals forces. The dynamical

stability of the structure has been confirmed by the absence of imaginary frequencies in the phonon dispersion (see Figure S1). Among 15 zone center phonon branches (12 optical and 3 acoustic) of Bi_2Te_3, 6 of them are Raman active and 6 are infrared (IR) active modes. The irreducible representation for the zone center phonons can be written as $\Gamma = 2E_g + 2A_{1g} + 2E_u + 2A_{1u}$, consistent with the point group symmetry D_{3d} [28]. Here, in-plane E_g and out-of-plane A_{1g} modes are Raman active, whereas E_u and A_{1u} are IR active mode [33]. The phonon dispersion and calculated Raman active modes of the monolayer Bi_2Te_3 (see Figure S1b) agree well with observed Raman shifts at 106.19 cm^{-1} (E_g) and 138.26 cm^{-1} (A_{1g}) from polarization-dependent Raman scattering (see Figure1(b)).

The irreducible representation of the vibrational modes of the $FePS_3$ monolayer can be written as $\Gamma = 8A_g + 6A_u + 7B_g + 9B_u$ consistent with the C_{2h} point group symmetry of the experimental structure. Among 30 vibrational modes, the A_g and B_g modes are Raman-active [34], three modes are acoustic, and the remaining ones are IR-active. The appearance of negative frequencies (imaginary modes) (see Figure S2a) on the phonon dispersion of the $FePS_3$ monolayer is likely due to the symmetry along the ferromagnetically coupled zigzag chains of Fe atoms [35]. Introducing symmetry-breaking in that direction leads to a strong structural distortion as two Fe-Fe bond lengths along the zigzag chains are no longer equal (2.78 and 3.73 Å, respectively). This is in contrast to the experimentally determined crystal structures, where ferromagnetically coupled zig-zag chains have a single Fe-Fe bond length of 3.32Å. Besides, the point group symmetry of this distorted structure is reduced to C_s, and the lack of centering in the structure doubled the number of vibrational modes of the $FePS_3$ monolayer. The phonon dispersion of this low-symmetry distorted structure is shown in Figure S2 (b), and as expected, the imaginary modes no longer exist. The higher wavenumber modes ($\geq$ 250 cm^{-1}), depicted in Figure 1(c) as SP1 (250 cm^{-1}), SP2 (280 cm^{-1}), and SP3 (380 cm^{-1}), are mostly attributed to the molecular-like vibrations from $(P_2S_6)^{4-}$ bipyramid structures, whereas the low-frequency peaks, zone folded phonons ($\leq$ 110 cm^{-1}) and magnons ($\sim$ 120 cm^{-1}), are from vibrations including Fe atoms [26, 29].

Next, we investigated temperature-dependent Raman scattering down to 5 K on HS-1, (see figure 1(a) for reference locations). In case of the heterostructure (HS-1), variation of the classified peaks at low temperature (T = 5 K) from the room temperature data in terms of peak position, full-width-half-maxima (FWHM), and the intensity can be read by the naked eye and may reveal contributions of phonon anharmonicity and spin-phonon coupling (see Figure 1(b)).

At the heterostructure region, there may be a significant coupling between the adjacent peaks,

as in between broad peak of $FePS_3$ (denoted as zone folded phonon (ZP) mode around 108 cm^{-1}) and characteristic E_g^2 mode (designated as E1 in Figure 1(b)) of Bi_2Te_3, which are characteristic phonon modes of individual compounds. Deconvolution of the hybrid peak around 110 cm^{-1} into two Lorentzian curves confirms that the broad ZP peak of $FePS_3$ becomes sharply peaked (100 times at 5 K) in presence of the underneath Bi_2Te_3 layer. Note that the disappearance of the broad peak around 100 cm^{-1} in the overlapping region at low temperature ($\sim$ 100 K) is remindful of the pristine $FePS_3$, as reported in [26]. To investigate the temperature dependent phonon behavior, the frequency (ω) and the linewidth (Γ) are extracted from the respective Lorentzian fits to specific phonon modes and were fit by symmetric three phonon coupling model (see Figure 2-3) [36]:

$$\omega(T) = \omega_1 + \frac{\omega^{'} - \omega_1}{1 + exp[\frac{T-T_0}{dT}]} \tag{1}$$

$$\Gamma = \Gamma_0 \left(1 + \frac{1}{exp(\frac{hc\bar{\nu_1}}{k_B T}) - 1} + \frac{1}{exp(\frac{hc\bar{\nu_2}}{k_B T}) - 1}\right) \tag{2}$$

Here, the parameters $\omega^{'}$ and ω_1 represent the top and bottom of the fitted sigmoidal curve, respectively; T_0 is the center point, and dT controls the width of the curve. h and k_B are the Planck and Boltzmann constants, respectively, c is the speed of light and T is the temperature. Γ_0 is the asymptotic value of the linewidth at zero temperature. $\bar{\nu_1}$ and $\bar{\nu_2}$ are two acoustic phonon modes with different wavenumbers with opposite wavevector.

In the isolated Bi_2Te_3 (see the inset of Figure 3(a)), no phonon anomaly was observed in the peak position and linewidth of the phonon modes, possibly due to the dominant phonon-phonon scattering [27]. The observed anharmonic behaviour is independent of the excitation wavelength [27], different structural form (bulk single crystal [37], nanowires, nanoribbons [38] etc.), and the thickness [27, 39] of Bi_2Te_3 (see Supplemental Table VIII). The behavior can simply be described by the above mentioned symmetric three-phonon coupling model [40] where a zone centre optical phonon decays into two acoustic phonons with equal energies and opposite momenta. Note that the fitting of the temperature dependent peak positions of the in-plane and out-of- plane phonon modes of isolated Bi_2Te_3 (see inset of Figure 3(a),(c)) and $FePS_3$ connected to the heterostructure (HS-1) is depicted in the Supplementary Information (Figure S3) [41].

In case of $FePS_3$, in the heterostructure (HS-1), at/around 65 K, SP1-SP3 modes show deviation from the anharmonic fit for each of the phonon frequencies [see Figure 2(a),(c),(e)]. Note that antiferromagnetic ordering sets in (T_N) at 120 K, irrespective of the thickness of the $FePS_3$

flake [26]. Also, no such changes were detected for the linewidth, may be due to the insignificant contribution of spin-phonon interaction to the phonon relaxation process [42]. The nature of the temperature dependent linewidth also suggests that the effect of phonon-impurity scattering, and electron-phonon interaction can be ruled out, as discussed in [28], whereas the violation of three phonon anharmonic decay model was observed in the linewidth of $FePS_3$ spin-phonon coupled modes (see figure 2(b),(d)) in the heterostructure due to Bi_2Te_3 underneath.

Noticeably, in the Bi_2Te_3/$FePS_3$ heterostructure (HS-1), the enhancement of the intensity in all the Raman modes of $FePS_3$, compared to the isolated flake, can be explained by the electron transfer at the Bi_2Te_3/$FePS_3$ interface. Adopting a simple model where the interface has been treated as a metal (Bi_2Te_3 is sufficiently n doped with $n \sim 10^{19}$ cm^{-3}) [43] - semiconductor ($FePS_3$ with bandgap 1.60 eV) junction, band alignment, depicted in Figure S4, indicates that the electrons will be transferred from $FePS_3$ into the Bi_2Te_3. The barrier ($E_{bar} \sim 1.17$ eV) formed at the interface, which is the difference between the work functions of the Bi_2Te_3 ($\phi_{BT} \sim 5.30$ eV) [44] and the $FePS_3$ ($\phi_{FPS} \sim 4.13$ eV), is less than the excitation wavelength (2.62 eV). Consequently, available transitions for the Raman scattering may involve real energy levels which drastically enhances the intensity of the characteristic Raman modes of $FePS_3$ [45].

One-magnon mode (M) at 120 cm^{-1} at a temperature ($T_M \sim 60$ K) was observed in $FePS_3$. Softening of this magnon mode appears at 30 K with $\triangle\omega \sim 4$ cm^{-1} in $FePS_3$ connected to heterostructure (HS-1) (see figure S5(a)) while, this anomaly occurs at 15 K [Fig.2(f)] with very small $\triangle\omega \sim 0.56$ cm^{-1} due to Bi_2Te_3 underneath, in the heterostructure [26, 29]. Additionaly, magnetic field dependent Raman scattering at 4 K offers an insightful observation on the spliiting of the magnon mode in the heterostructures. By applying a magnetic field perpendicular to the ab plane of the HS-1, magnon-gap excitation can be splitted into two components (linear in B with g-factor close to 2.15) following the easy-axis antiferromagnetic properties which has already been reported by Vaclavkova *et al.* for the isolated $FePS_3$ [29]. Moreover, no such changes in the strength of magnon-phonon coupling (~ 3 cm^{-1}) was observed in the case of heterostructure. In due course, while applying magnetic field parallel to the ab plane of the HS-1, magnon mode of $FePS_3$ splits at much lower magnetic field (~ 9 T) compared to in-plane splitting field in isolated $FePS_3$ (~ 16 T) reported in [29]. Note that the Raman modes of isolated Bi_2Te_3 shows no magnetic field dependence in either configuration, as also reported in previous studies [27] (see Supplemen-

tary Information Figure S24, Table IX) . To understand the reduction of the external "in-plane" magnetic field required for the splitting of the magnon in the HS-1, one can speculate the effect of the time-independent antidamping torque which may generate further "in-plane" field-like effect predicted for antiferromagnetic topological insulators with preserving the gapless states in TI [46] (see Supplementary Information Figure S24 , Table IX). Besides, to inspect the origin of the possible magnon temperature reduction in hybrid $FePS_3$, the spin wave stiffness constant (D) which is linked to the long wavelength limit of the acoustic mode of magnon dispersion can be determined. Our noncollinear density functional theory (ncDFT) calculations (see the methodology for computational details) predict that monolayer $FePS_3$ has spin wave stiffness of 245 meVÅ^2. Interestingly, D value gets reduced to 158 meVÅ^2 for $FePS_3$ deposited onto six quintuple layer (6QL) of Bi_2Te_3.

Figure 3 presents the temperature dependence of the in-plane and the out-of-plane phonon modes of Bi_2Te_3 in the heterostructure. Unlike pristine Bi_2Te_3 (see the inset of Figure 3a and 3c) [27], at/around 60 K, respective phonon modes, E_g^2 (see Figure 3a) and A_{1g}^2 (see Figure 3c), show clear deviation ($\triangle\omega_{5K}$) of 1.56 cm^{-1} and 1.62 cm^{-1} from the anharmonic fit, respectively. Regarding linewidth, while E_g^2 mode shows slight deviation ($\sim$ 0.56 cm^{-1}) in the phonon behaviour around 60 K (see Figure 3b), no such abrupt changes were observed for A_{1g}^2 mode (see Figure 3d). Theoretically, spin-phonon coupling can be introduced as spin susceptibility (χ_M) in the phonon self energy (SE) which consists of the real (frequency shift) and the imaginary part (line broadening) ($\Delta(\omega_j(q),T) + i\Gamma(\omega_j(q),T)$), analogous to modification due to electron-phonon coupling [27]. On account of this, from our result, a clear departure of χ_M from the usual phonon behavior in the Bi_2Te_3 can be identified at/around 60 K in the heterostructure (see Figure S6(a), (b)). Thickness dependent Raman measurements were done on Bi_2Te_3/$FePS_3$ heterostructures (HS-2, HS-3) with temperature ranging from 5 K to 300 K. The coupling strength was observed to be high for the heterostructure consisting of thick-layer Bi_2Te_3 and $FePS_3$. Strength of spin-phonon coupling of Raman modes of Bi_2Te_3 decreases with the reduction of thickness (see fig. S8) of individual material as observed in [47]. In the heterostructure, with reduced thickness, surface phonon polariton is red shifted and as a result, it becomes off-resonant with antiferromagnetic magnon, which, in-turn, reduces the coupling strength of the hybridized quasi-particle. The deviation from the phonon anharmonicity $\Delta\omega$ (related to square of magnetization) decreases with lowering the thickness of Bi_2Te_3 and $FePS_3$ in heterostructures. In the case of HS-1, the value of $\Delta\omega$ is close to 1.21 which is higher than the recorded values for HS-2 ($\Delta\omega \sim 0.69$) and HS-3 (($\Delta\omega \sim 0.57$) for the in-plane and out-of-plane Raman modes of Bi_2Te_3. The deviation ($\Delta\omega$) is more prominent

in out-of-plane mode (A^2_{1g}) of Bi_2Te_3 in case of few layer heterostructure (see fig. S8(d)) since Bi and Te atoms vibrate perpendicularly to the layer surface for A^2_{1g} mode [48]. The coupling strength decreases but the characteristic temperature for spin-phonon coupling of Bi_2Te_3 remains invariant ($\sim$ 60 K) with reduction of thickness (see fig. S8). The robustness of spin-phonon coupling of Bi_2Te_3 in Bi_2Te_3/$FePS_3$ heterostructure (HS-4, HS-5) could be destroyed by inserting hexagonal boron nitride (hBN) in between Bi_2Te_3 and $FePS_3$ (see Figure 5). The insulating nature of the $FePS_3$ with highly transparent hBN [49] in the middle of the stacked assembly make the laser penetration depth very large (also recognizable under optical microscope), which in turn facilitates the recording of the characteristic Raman modes of individual materials even in bulk thicknesses (see Figure 5(b)). No such phonon anomaly (independent of the thickness of hBN) was observed in the in-plane and out-of-plane Raman modes of Bi_2Te_3 (see Figure 5(c), (d)), similar to the case of isolated Bi_2Te_3.

Typical example of magnetic proximity effect [50–53] is the extension of the spin order beyond the interface of diluted magnetic semiconductors (DMS), namely (Ga, Mn)As, and Fe overlayer through an anti-parallel alignment. Avoiding the effect of diffusion/seggregation in DMS subsystem, nontrivial surface state of TI in contact with FMI can be understood from the propagation of spin-polarized charge carriers resulting in building up finite spin polarization close to the interface [54]. Moreover, presence of the TI's conducting surface states is crucial for the spin polarized charge transfer [53, 55]. On a related note, diffusion of the magnetic atoms (*e.g* Eu atoms in EuS) into the first QL of TI (*e.g* Bi_2Se_3) during the growth of the heterostructure can be the origin of "interface ferromagnetism", as reported in [56]. But, in the concerned study, heterostructure has been formed *via* stamping of one vdW material onto another, eliminating the possibility of diffusion which usually happens during the thin film growth [57]. Interfacial ferromagnetism remains evident up to room temperature in Bi_2Se_3/EuS heterostructure. Significant enhancement of T_C was observed at the interface arising from large spin–orbit interaction and spin–momentum locking of the topological insulator surface [58]. In Bi_2Te_3/Fe_3GeTe_2 heterostructure, T_C enhances up to 400 K, which is attributed to the interfacial exchange coupling effect between Bi_2Te_3 and Fe_3GeTe_2, which induces the enhancement of T_C for the 2D ferromagnetism [59]. The enhancement of T_C of $Cr_2Ge_2Te_6$ from 65 K to 150 K was observed in W/$Cr_2Ge_2Te_6$ heterostructure due to the formation of W-Te bonding at the interface [60]. In the stacked structure, strain engineering may enhance the T_C by raising the exchange energy between the cation sites which may be mediated by the polarized anion atoms [59]. But even for the fully epitaxial vdW heterostructure (*e.g* $Fe_xCu_{1-x}Se$

and Bi_2Te_3), lattice mismatch, as large as 20%, may occur through van der Waals bonding across the interface [61]. For a typical sample size of sub-micrometer length scale, structural, chemical and electronic analysis of the heterointerface as formed in the vdW stacking, can be probed by low-energy electron microscopy (LEEM), which is beyond the scope of the current work [62, 63]. However, in our micromanipulated vdW Bi_2Te_3/$FePS_3$ heterostructure, possible strain has been calculated as low as 0.5%.

The magnetic and electronic properties of the Bi_2Te_3/$FePS_3$ heterostructure have been investigated by performing DFT calculations using a supercell containing both individual layers coupled weakly by the vdW interaction (see methods for details). Since the point group symmetry (D_{3d}) remains invariant with the thickness of Bi_2Te_3, we have considered Bi_2Te_3 monolayer for our calculations to save computational time. Note that no significant Raman shift was observed in the in-plane phonon characteristic mode (E_g^2) of Bi_2Te_3, whereas, out-of-plane Raman mode (A_{1g}^2) shows a maximum shift of 6 cm^{-1} with thickness [48, 64, 65] (See Supplementary Information Table IV, Table VII). In the context of the current study, temperature dependent phonon anomaly as detected from the deviation from anharmonicity, in phonon frequency for a certain thickness is conceptually different from the thickness dependent variation of Raman shift. Contrastingly, all phonon modes of $FePS_3$ hardly show any Raman shift with decreasing thickness down to monolayer (see Supplementary Information, Figure S23, Table VI). It is worth mentioning that $FePS_3$ exhibits layer thickness independent transition temperature ($T_N \sim 120$ K) from bulk to monolayer [66]. In this framework, the S-termination of the $FePS_3$ layer (on top of the Bi_2Te_3 layer) is energetically the most stable configuration, and the stoichiometry of each individual layer is also maintained. Interestingly, the magnetic ground state (z-AFM order; cf. (Fig. 4a) of the $FePS_3$ layer remains unchanged even in this heterostructure set-up. The robustness in AFM order of $FePS_3$ compound [66] from bulk to monolayer to heterostructure is promising for device applications. We obtain $\sim 3.5\ \mu_B$ magnetic moment at the Fe^{2+} sites, whereas the other atoms have negligibly small moments ($< 0.1\ \mu_B$). Furthermore, the nature of the spin anisotropy of the interface $FePS_3$ layer was determined from our calculated magnetocrystalline anisotropy energies (MAE). The obtained MAE ($E_{in-plane}$-E_z) value 1.31 meV/f.u. of the $FePS_3$ layer indicates the easy axis (out-of-plane) of magnetic anisotropy of the system. Relatively large MAE value [67] originates from the strong spin-orbit coupling (SOC) in the Bi_2Te_3/$FePS_3$ heterostructure. In contrast, magnetic shape anisotropy (MSA), which represents the anisotropic dipolar interaction of free magnetic poles and tends to align magnetic moments parallel to surfaces, only plays a sig-

nificant role when SOC is weak [67]. MSA values are generally in the order of μeV, and thus, they are negligible for Bi_2Te_3/$FePS_3$ heterostructure . Therefore, the long-range order observed in the Bi_2Te_3/$FePS_3$ heterostructure is primarily governed by MAE. The GGA+U+SOC electronic structures (Fig 4b) of the Bi_2Te_3/$FePS_3$ heterostructure reveal that the system is a narrow band-gap (0.25 eV) semiconductor. The atom-projected density of states (DOS) shows that the bands below the Fermi level (FL) are predominantly occupied by Bi and Te valence states, and there is a strong hybridization between the Fe d levels and the valence-band orbitals of Bi_2Te_3. Since this hybridization is spin-dependent, the proximity exchange could be significant [68] and may lead to gaped surface states as opposed to the metallic surface states of isolated Bi_2Te_3 (see Figure S5(b). Note that scanning tunnelling spectroscopy on Bi_2Te_3/$FePS_3$ heterostructure may invoke insights into the atomistic origin of the proximitized magnetic ordering which is beyond the scope of the current work.

To understand the microscopic origin of the reduction of T_{N} of $FePS_3$ in the heterostructure, we calculate the interface AFM exchange (J_{int}) by using the energy difference between FM and z-AFM spin configurations after mapping them to the Heisenberg model $H = J_{int} \sum_{i>j} S_i \cdot S_j$ (cf. supplemental materials S7 for details). We estimate J_{int} to be 69 K, lower than the AFM exchange J_{ML} of the $FePS_3$ monolayer (110 K). The lowering of AFM exchange in the Bi_2Te_3/$FePS_3$ heterostructure is consistent with the experimentally observed trend in T_{N}. In $FePS_3$, Fe atoms are in an edge-sharing octahedral environment with their neighboring S, and in this case, the Fe-S-Fe bond angle is close to 90^o. In this situation, direct d-d hopping, which gives rise to an antiferromagnetic exchange competes with the FM superexchange [69, 70]. In the 0.5% bi-axial strained structure of the $FePS_3$ monolayer, the Fe-S-Fe bond angle is $\sim 10^o$ smaller than the unstrained structure, whereas the Fe-Fe bond length remains almost the same. Due to this reason, the effective AFM interaction (J_{ML} = 80 K) of the strained $FePS_3$ monolayer gets weakened by the enhancement of FM superexchange. In Bi_2Te_3/$FePS_3$ monolayer, we also observe a similar trend with higher reduction in Fe-S-Fe bond angles , and thus the overall AFM exchange becomes much weaker. Therefore, the interfacial strain which leads to smaller Fe-S-Fe bond angles could primarily attribute to the lowering of J_{int} in the heterostructure system. The nature of the strain demonstrated in the calculations corresponds to compressive biaxial strain for the $FePS_3$ monolayer. Similar strain effects due to the lattice mismatch at the vdW interface between Bi_2Te_3 and $FePS_3$ was observed (See Supplementary Information Table V). In case of $FePS_3$ connected to the

heterostructure, reduction of T_N was observed at/around 65 K (see supplementary information Fig. S3). The interfacial strain arises due to the lattice mismatch, which propagates laterally through the layer at a certain distance ($\sim$ 100 nm) from the edge of the interface and decreases with the distance as reported in previous computational studies [71]. Similar hetero-bonding effect due to strain has been detected in WSe_2-MoS_2 heterostructure *via* scanning probe microscopy [72]. In our case, the strain propagation is the most probable origin of the reduced T_N in $FePS_3$ connected to the heterostructure (beyond overlapping region), as depicted in the supplemental figure (Fig. S3). A proper mapping of the two-dimensional strain tensor (in-plane) would be necessary to understand the precise extension of the decay. Further studies, like spin-polarized scanning probe microscopy, are required for an atomistic picture of strain distribution. In the current work, in spite of the reduction in T_N, increment of the sublattice magnetization of $FePS_3$ in case of the heterostructure can be observed as $\Delta\omega$ value is enhanced by 4 times compared to isolated $FePS_3$ which may result in better device performance, may be realized *via* magneto-transport measurement.

A sharp decrease in the Raman shift is observed at 30 K (see figure 3(a),(c)) in both modes of Bi_2Te_3 in the heterostructure. This could be understood from the temperature-dependent antiferromagnetic order parameter. The magnetization of the bulk state falls faster than the surface states with temperature (see figure S9 (a),(b)) as reported in [73]. In mean field approximation, one can relate $\Delta\omega$ to magnetization as $\Delta\omega(T) \propto \frac{M^2(T)}{M^2_{max}}$. Magnetization ($M$) is plotted with temperature for the phonon modes of Bi_2Te_3 in the heterostructure (see figure S9 (a),(b)) and fit with $M \approx |(1 - \frac{T}{T_N})|^\beta$ equation, where β is the critical exponent. β value at 60 K (0.15) corrborates with 2D Ising model, the origin of the surface magnetic contribution comes from $FePS_3$ and the β value at 30 K (0.35) corresponds to 3D Heisenberg model, responsible for bulk contribution. The exponent value, β for isolated $FePS_3$ and $FePS_3$ in the heterostructure are close to the mean field (see figure S9(c)). With decreasing the Bi_2Te_3 layers, proximity induced bulk magnetization (related to $\Delta\omega$) in Bi_2Te_3 decreases and as a result coupling strength at the interface was also reduced. Induced bulk magnetization reduces more than 4 times in Bi_2Te_3 when thickness of Bi_2Te_3 reduces from $\sim$ 500 nm (HS-1) to $\sim$ 12 nm (HS-II) (see supplementary figure, Fig. S25).

Now we turn to discuss the spin-phonon coupling of the Bi_2Te_3/$FePS_3$ heterostructure. This complex heterostructure has a P_1 space group and C_1 point group symmetry, and due to having a large number of atoms in the supercell, the phonon calculation of this heterostructure is very expensive. Therefore, we calculate the phonons of individual monolayers and combine them together

to understand the Raman data of the Bi_2Te_3/$FePS_3$ heterostructure. The spin-phonon coupling parameter of the $FePS_3$ monolayer has been estimated from the shift in Γ-phonons due to a change in magnetic order from z-AFM to FM. The Raman active modes corresponding to both magnetic order and relative change in phonon frequencies ($\Delta_\lambda^{rel} = \frac{\omega_{FM} - \omega_{z-AFM}}{\omega_{z-AFM}}$) are listed in Supplemental Table 2. The significant change in phonon frequencies due to a change in magnetic order indicates the strong coupling between magnetic and lattice degrees of freedom in the $FePS_3$ monolayer.

In particular, 115 cm^{-1} and 141 cm^{-1} A_g modes of $FePS_3$ show significant spin-phonon couplings. Interestingly, the frequencies of these two modes are close to the phonon frequency of E_g and A_{1g} modes of Bi_2Te_3 (Supplemental Table 1). There is a possibility that the Bi_2Te_3 modes would couple to phonons of similar frequencies of $FePS_3$ due to resonance, and the hybrid modes appear in the Raman spectrum. Such coupling phenomena were reported in earlier literature [74], where magnon excitations with Raman-allowed symmetries couple to similar frequency phonon modes showing strong spin-phonon coupling. In order to illustrate the temperature dependence of the hybrid modes, we consider the Ginzburg-Landau (GL) theory formalism [74]. Due to the spin-phonon coupling, the phonon frequency will vary with temperature below T_N as the z-AFM order sets in, and the modified phonon frequency is given by the formula:

$$\omega_\lambda = 2 \triangle_\lambda m^2 + \sqrt{\omega_{0\lambda}^2 + 4 \triangle_\lambda^2 m^4} \tag{3}$$

where $m \sim (1 - \frac{T}{T_N})^\beta$ is the magnetic order parameter, $\omega_{0\lambda}$ is the high-temperature ($T \geq T_N$) phonon frequency the λ_{th} phonon mode, and $\triangle_\lambda$ is the spin-phonon coupling parameter derived from the DFT calculations. The temperature dependence of the coupled hybrid modes is shown in Fig 4(c-d). One can see both phonon frequencies increase with increasing temperature which qualitatively agrees with the trend observed in experiments. The spin-phonon coupled hybrid modes in the heterostructure could be attributed to the phonon-resonance phenomenon due to the proximity effect.

CONCLUSION

In conclusion, we report a proximate AFM order in Bi_2Te_3, a topological insulator, by investigating the temperature-dependent Raman spectroscopy of Bi_2Te_3 (TI)- $FePS_3$ (AFM with $T_N \sim$ 120 K) stacked vdW heterostructure down to 5 K. Unlike isolated Bi_2Te_3, a deviation from the usual phonon anharmonicity in Raman modes corresponding to Bi_2Te_3 in the heterostructure was

observed at 60 K and can be correlated to antiferromagnetic proximity induced spin-phonon coupling. The strength of spin-phonon coupling decreases with the reduction of thickness of Bi_2Te_3 and $FePS_3$ in heterostructure, but the characteristic temperature for spin-phonon coupling remains invariant ($\sim$ 60 K). The robust spin-phonon coupling in Bi_2Te_3 could be destroyed by placing hBN in between Bi_2Te_3 and $FePS_3$ in the heterostructure. Also, a reduction of T_N to 65 K of hybrid $FePS_3$ was identified, possibly due to the interfacial strain which leads to smaller Fe-S-Fe bond angles as corroborated by DFT calculations. The current study on the spatial variation of spin-phonon coupling at the interface of vdW magnet-TI heterostructure may be crucial for the future spin logic devices.

Methods

Sample preparation

Binary Bi_2Te_3 single crystal was grown through solid-state reaction method by using box furnace. Bismuth powder (Alfa Aesar, purity 99.999%) , Tellurium powder (Alfa Aesar , purity 99.999%) were mixed in proper stoichiometric ratio and sealed into a quartz ampoule under vacuum($\approx 10^{-5}$ mbar). The ampoule was then placed at the centre of the furnace and heated at 700° C for seven days [30].

Computational Details

Density functional theory (DFT) calculations have been performed by using a plane-wave basis set with a kinetic energy cutoff of 400 eV and projector augmented-wave [75, 76] potentials as implemented in the Vienna Ab initio Simulation Package (VASP) [77, 78]. For the exchange-correlation functional, the Perdew-Burke-Ernzerhof (PBE) [79] version of the generalized gradient approximation (GGA) has been used. In our calculations, the spin-polarized case for $FePS_3$ and the non-spin-polarized case for Bi_2Te_3 have been considered. During structural relaxations, the positions of the ions were relaxed until the Hellman-Feynman forces became less than 0.001 eV/Å. Correlation effects for Fe d electrons have been incorporated within GGA+U [80] approach, and an effective on-site Coulomb repulsion U_{eff} = 3 eV, which is within the range of U values used for [81–83] has been considered. In addition, spin-orbit coupling (SOC) was included in our calculations to get the correct electronic band dispersion for Bi_2Te_3 and estimate the magnetic anisotropy for $FePS_3$. Phonons were calculated using the density functional perturbation theory (DFPT) [84] as implemented in the PHONOPY [85].

The Bi_2Te_3-$FePS_3$ heterostructure has been constructed within the Quantum ATK framework [86]. The surface matching algorithm described in ref [87] was utilized to obtain low-strain

hetero-interfaces. For this heterostructure, the mean absolute strain values on both the monolayer surfaces were calculated as $\sim$0.5%. The composite supercell was then fully relaxed within the vdW correction method DFT-D3 [88] until forces on atoms became less than 0.02 eV/Å. The reciprocal space integration was carried out with a Γ centered k-mesh of $8 \times 8 \times 2$ for Bi_2Te_3 bulk, $12 \times 12 \times 1$ for Bi_2Te_3 single layer, $12 \times 8 \times 1$ for $FePS_3$ monolayer, and $2 \times 2 \times 1$ for the Bi_2Te_3-$FePS_3$ heterostructure.

For Magnon Stiffness Calculation, We employ the interface builder in the QuantumATK package [86] to construct a unit cell of the 1ML-$FePS_3$/6QL-Bi_2Te_3 heterostructure with 2×2 supercell of $FePS_3$ and $\sqrt{7} \times \sqrt{7}$ supercell of Bi_2Te_3. Spin wave stiffness constant D of 1ML-$FePS_3$ /6QL-Bi_2Te_3 heterostructure is calculated using Green's function (GF) formalism of Ref. [89], as implemented in QuantumATK package [86]. The Kohn-Sham Hamiltonian of density functional theory (DFT), as the input of GF formalism, is obtained from noncollinear DFT calculations using the Perdew-Burke-Ernzerhof (PBE) parametrization [90] of the generalized gradient approximation (GGA) to the exchange-correlation functional, as implemented in QuantumATK package [86]; norm-conserving fully relativistic pseudopotentials of the type PseudoDojo-SO [86, 91] for describing electron-core interactions; and the Pseudojojo (medium) numerical linear combination of atomic orbitals (LCAO) basis set [91]. The energy mesh cutoff for the real-space grid is chosen as 101 Hartree, and the k-point grid $6 \times 6 \times 1$ is used for the self-consistent calculations. Periodic boundary condition is used for the self-consistent calculations, and a 15Å vacuum is placed on the top of heterostructure in order to remove interaction between the consecutive periodic image.

Acknowledgments

The authors would like to thank Dr. Vasant Sathe, Prof. K Sengupta, Dr. Marek Potemski, Dr. Clément Faugeras, Prof. Achintya Singha, Mr. Somsubhra Ghosh, Dr. Mintu Mondal, and Dr. Devajyoti Mukherjee for fruitful discussion. SMaity and TK are grateful to DST-INSPIRE for their fellowships. D.D. and L.Y. gratefully acknowledge the U.S. DOE, Office of Science, Office of Basic Energy Sciences, under Award No. DE-SC0021127 for financial assistance and Advanced Computing Group of the University of Maine System for providing computational resources for this work. SMasanta is grateful to Council of Scientific & Industrial Research (CSIR), New Delhi, for the financial support through the award of NET-SRF (File No: 09/015(0531)/2018-EMR-I). The authors are thankful to the facilities at UGC-DAE-CSR-Indore. Magneto-Raman scattering at low temperature were performed at LNCMI, European Magnetic Field Laboratory at Grenoble under the project GSC08-119. SMaity would like to thank Ms. Diana Vaclavkova, Ms. Anushree

Dey, Mr. Sanjib Naskar, Mr. Rahul Paramanik and Mr. Soumik Das. MP and BD is grateful to IACS for the fellowship. SD acknowledges the financial support from DST-SERB grant No. ECR/2017/002037, SCP/2022/000411 and CRG/2021/004334. SD also acknowledges support from the Central Scientific Service (CSS) and the Technical Research Centre (TRC), IACS, Kolkata.

---

[1] S. V. Eremeev, V. N. Men'shov, V. V. Tugushev, P. M. Echenique, and E. V. Chulkov, Phys. Rev. B **88**, 144430 (2013).

[2] M. Liu, J. Zhang, C.-Z. Chang, Z. Zhang, X. Feng, K. Li, K. He, L.-l. Wang, X. Chen, X. Dai, Z. Fang, Q.-K. Xue, X. Ma, and Y. Wang, Phys. Rev. Lett. **108**, 036805 (2012).

[3] Y. L. Chen, J.-H. Chu, J. G. Analytis, Z. K. Liu, K. Igarashi, H.-H. Kuo, X. L. Qi, S. K. Mo, R. G. Moore, D. H. Lu, M. Hashimoto, T. Sasagawa, S. C. Zhang, I. R. Fisher, Z. Hussain, and Z. X. Shen, Science **329**, 659 (2010), https://www.science.org/doi/pdf/10.1126/science.1189924.

[4] J. Henk, M. Flieger, I. V. Maznichenko, I. Mertig, A. Ernst, S. V. Eremeev, and E. V. Chulkov, Phys. Rev. Lett. **109**, 076801 (2012).

[5] T. K. Dalui, P. K. Ghose, S. Majumdar, S. K. Mahatha, F. Diekmann, K. Rossnagel, R. Tomar, S. Chakraverty, A. Berlie, and S. Giri, Phys. Rev. B **103**, 064428 (2021).

[6] Y. Fan, X. Kou, P. Upadhyaya, Q. Shao, L. Pan, M. Lang, X. Che, J. Tang, M. Montazeri, K. Murata, L. Chang, M. Akyol, G. Yu, T. Nie, K. Wong, J. Liu, Y. Wang, Y. Tserkovnyak, and K. Wang, Nature Nanotechnology **11**, 352 (2016).

[7] I. Lee, C. K. Kim, J. Lee, S. J. L. Billinge, R. Zhong, J. A. Schneeloch, T. Liu, T. Valla, J. M. Tranquada, G. Gu, and J. C. S. Davis, Proceedings of the National Academy of Sciences **112**, 1316 (2015), https://www.pnas.org/doi/pdf/10.1073/pnas.1424322112.

[8] I. Vobornik, U. Manju, J. Fujii, F. Borgatti, P. Torelli, D. Krizmancic, Y. S. Hor, R. J. Cava, and G. Panaccione, Nano Letters **11**, 4079 (2011), pMID: 21861485, https://doi.org/10.1021/nl201275q.

[9] Q. I. Yang, M. Dolev, L. Zhang, J. Zhao, A. D. Fried, E. Schemm, M. Liu, A. Palevski, A. F. Marshall, S. H. Risbud, and A. Kapitulnik, Phys. Rev. B **88**, 081407 (2013).

[10] M. Blei, J. Lado, Q. Song, D. Dey, O. Erten, V. Pardo, R. Comin, S. Tongay, and A. Botana, Applied Physics Reviews **8** (2021).

[11] Q. He, X. Kou, A. Grutter, L. Pan, X. Che, Y. Liu, T. Nie, S. Disseler, B. Kirby, I. Ratcliff, Q. Shao,

K. Murata, Y. Fan, M. Montazeri, J. Borchers, K. Wang, and B. Zhang, Nature materials **16** (2016).

[12] A. K. Geim and I. V. Grigorieva, Nature **499**, 419 (2013).

[13] H. X. Yang, A. Hallal, D. Terrade, X. Waintal, S. Roche, and M. Chshiev, Phys. Rev. Lett. **110**, 046603 (2013).

[14] Z. Qiao, W. Ren, H. Chen, L. Bellaiche, Z. Zhang, A. H. MacDonald, and Q. Niu, Phys. Rev. Lett. **112**, 116404 (2014).

[15] P. Wei, S. Lee, F. Lemaitre, L. Pinel, D. Cutaia, W. Cha, F. Katmis, Y. Zhu, D. Heiman, J. Hone, J. S. Moodera, and C.-T. Chen, Nature materials **15**, 711—716 (2016).

[16] J. C. Leutenantsmeyer, A. A. Kaverzin, M. Wojtaszek, and B. J. van Wees, 2D Materials **4**, 014001 (2016).

[17] S. Geprägs, S. Meyer, S. Altmannshofer, M. Opel, F. Wilhelm, A. Rogalev, R. Gross, and S. T. B. Goennenwein, Applied Physics Letters , 262407 (2012), https://doi.org/10.1063/1.4773509.

[18] J. Qi, X. Li, Q. Niu, and J. Feng, Phys. Rev. B **92**, 121403 (2015).

[19] L. Xu, M. Yang, L. Shen, J. Zhou, T. Zhu, and Y. P. Feng, Phys. Rev. B **97**, 041405 (2018).

[20] G. Yang, J. Li, H. Ma, Y. Yang, C. Li, X. Mao, and F. Yin, Phys. Rev. B **98**, 235419 (2018).

[21] K. Zollner, P. E. Faria Junior, and J. Fabian, Phys. Rev. B **100**, 085128 (2019).

[22] B. Karpiak, A. W. Cummings, K. Zollner, M. Vila, D. Khokhriakov, A. M. Hoque, A. Dankert, P. Svedlindh, J. Fabian, S. Roche, and S. P. Dash, 2D Materials **7**, 015026 (2019).

[23] C. Lee, F. Katmis, P. Jarillo-Herrero, J. S. Moodera, and N. Gedik, Nature communications **7**, 1 (2016).

[24] L. Du, J. Tang, Y. Zhao, X. Li, R. Yang, X. Hu, X. Bai, X. Wang, K. Watanabe, T. Taniguchi, D. Shi, G. Yu, X. Bai, T. Hasan, G. Zhang, and Z. Sun, Advanced Functional Materials **29**, 1904734 (2019), https://onlinelibrary.wiley.com/doi/pdf/10.1002/adfm.201904734.

[25] A. Milosavljević, A. Šolajić, J. Pešić, Y. Liu, C. Petrovic, N. Lazarević, and Z. V. Popović, Phys. Rev. B **98**, 104306 (2018).

[26] A. Ghosh, M. Palit, S. Maity, V. Dwij, S. Rana, and S. Datta, Phys. Rev. B **103**, 064431 (2021).

[27] S. Buchenau, S. Scheitz, A. Sethi, J. E. Slimak, T. E. Glier, P. K. Das, T. Dankwort, L. Akinsinde, L. Kienle, A. Rusydi, C. Ulrich, S. L. Cooper, and M. Rübhausen, Phys. Rev. B **101**, 245431 (2020).

[28] B. Irfan, S. Sahoo, A. P. S. Gaur, M. Ahmadi, M. J.-F. Guinel, R. S. Katiyar, and R. Chatterjee, Journal of Applied Physics **115**, 173506 (2014), https://doi.org/10.1063/1.4871860.

[29] D. Vaclavkova, M. Palit, J. Wyzula, S. Ghosh, A. Delhomme, S. Maity, P. Kapuscinski, A. Ghosh, M. Veis, M. Grzeszczyk, C. Faugeras, M. Orlita, S. Datta, and M. Potemski, Phys. Rev. B **104**, 134437

(2021).

[30] M. Koyano, J. Tanaka, K. Suekuni, and T. Ariga, Journal of electronic materials **41**, 1317 (2012).

[31] A. Ghosh, M. Birowska, P. K. Ghose, M. Rybak, S. Maity, S. Ghosh, B. Das, S. Bera, S. Bhardwaj, S. Nandi, and S. Datta, Anisotropic magnetodielectric coupling in layered antiferromagnetic $feps_3$ (2022).

[32] A. Castellanos-Gomez, M. Buscema, R. Molenaar, V. Singh, L. Janssen, H. S. J. van der Zant, and G. A. Steele, 2D Materials **1**, 011002 (2014).

[33] J. Yuan, M. Zhao, W. Yu, Y. Lu, C. Chen, M. Xu, S. Li, K. P. Loh, and Q. Bao, Materials **8**, 5007 (2015).

[34] F. Kargar, E. A. Coleman, S. Ghosh, J. Lee, M. J. Gomez, Y. Liu, A. S. Magana, Z. Barani, A. Mohammadzadeh, B. Debnath, *et al.*, ACS nano **14**, 2424 (2020).

[35] A. Hashemi, H.-P. Komsa, M. Puska, and A. V. Krasheninnikov, The Journal of Physical Chemistry C **121**, 27207 (2017).

[36] J. Menéndez and M. Cardona, Physical Review B **29**, 2051 (1984).

[37] P. Mal, G. Bera, G. Turpu, S. K. Srivastava, A. Gangan, B. Chakraborty, B. Das, and P. Das, Physical Chemistry Chemical Physics **21**, 15030 (2019).

[38] D. Park, S. Park, K. Jeong, H.-S. Jeong, J. Y. Song, and M.-H. Cho, Scientific reports **6**, 19132 (2016).

[39] M. P. Singh, S. Ryntathiang, S. Krishnan, and P. K. Nayak, Current Chinese Science **1**, 453 (2021).

[40] P. Klemens, Physical Review **148**, 845 (1966).

[41] L. Casto, A. Clune, M. Yokosuk, J. Musfeldt, T. Williams, H. Zhuang, M.-W. Lin, K. Xiao, R. Hennig, B. Sales, *et al.*, APL materials **3**, 041515 (2015).

[42] M. Prosnikov, A. Smirnov, V. Y. Davydov, R. Pisarev, N. Lyubochko, and S. Barilo, Physical Review B **98**, 104404 (2018).

[43] T. Okuda, K. Nakanishi, S. Miyasaka, and Y. Tokura, Physical Review B **63**, 113104 (2001).

[44] E. Lee, J. Ko, J.-Y. Kim, W.-S. Seo, S.-M. Choi, K. H. Lee, W. Shim, and W. Lee, Journal of Materials Chemistry C **4**, 1313 (2016).

[45] G. B. Osterhoudt, R. Carelli, K. S. Burch, F. Katmis, N. Gedik, and J. S. Moodera, Phys. Rev. B **98**, 014308 (2018).

[46] S. Ghosh and A. Manchon, Phys. Rev. B **95**, 035422 (2017).

[47] D. Q. To, W. Wu, S. Bhatt, Y. Liu, A. Janotti, J. M. O. Zide, M. J. H. Ku, J. Q. Xiao, M. B. Jungfleisch, S. Law, and M. F. Doty, Phys. Rev. Mater. **7**, 045201 (2023).

[48] C. Wang, X. Zhu, L. Nilsson, J. Wen, G. Wang, X. Shan, Q. Zhang, S. Zhang, J. Jia, and Q. Xue, Nano Research **6**, 688 (2013).

[49] D. C. Nguyen, M. Kim, M. Hussain, I. Akhtar, B. A. Naqvi, M. A. Shehzad, J. Jung, Y. Seo, *et al.*, Nanotechnology **31**, 195701 (2020).

[50] C. Tang, Z. Zhang, S. Lai, Q. Tan, and W.-b. Gao, Advanced Materials **32**, 1908498 (2020).

[51] T. S. Ghiasi, A. A. Kaverzin, A. H. Dismukes, D. K. de Wal, X. Roy, and B. J. van Wees, Nature nanotechnology **16**, 788 (2021).

[52] W. Zhu, C. Song, L. Han, H. Bai, C. Chen, and F. Pan, Phys. Rev. B **108**, L100406 (2023).

[53] X. Chen, H. Bai, Y. Ji, Y. Zhou, L. Liao, Y. You, W. Zhu, Q. Wang, L. Han, X. Liu, *et al.*, Nature Electronics **5**, 574 (2022).

[54] F. Maccherozzi, M. Sperl, G. Panaccione, J. Minár, S. Polesya, H. Ebert, U. Wurstbauer, M. Hochstrasser, G. Rossi, G. Woltersdorf, *et al.*, Physical review letters **101**, 267201 (2008).

[55] W. Liu, L. He, Y. Xu, K. Murata, M. C. Onbasli, M. Lang, N. J. Maltby, S. Li, X. Wang, C. A. Ross, *et al.*, Nano letters **15**, 764 (2015).

[56] S. Eremeev, V. Men, V. Tugushev, E. V. Chulkov, *et al.*, Journal of Magnetism and Magnetic Materials **383**, 30 (2015).

[57] S. Liu, X. Yuan, Y. Zou, Y. Sheng, C. Huang, E. Zhang, J. Ling, Y. Liu, W. Wang, C. Zhang, *et al.*, npj 2D Materials and Applications **1**, 1 (2017).

[58] F. Katmis, V. Lauter, F. S. Nogueira, B. A. Assaf, M. E. Jamer, P. Wei, B. Satpati, J. W. Freeland, I. Eremin, D. Heiman, *et al.*, Nature **533**, 513 (2016).

[59] H. Wang, Y. Liu, P. Wu, W. Hou, Y. Jiang, X. Li, C. Pandey, D. Chen, Q. Yang, H. Wang, *et al.*, ACS nano **14**, 10045 (2020).

[60] W. Zhu, C. Song, L. Han, H. Bai, Q. Wang, S. Yin, L. Huang, T. Chen, and F. Pan, Advanced Functional Materials **32**, 2108953 (2022).

[61] A. Ghasemi, D. Kepaptsoglou, P. L. Galindo, Q. M. Ramasse, T. Hesjedal, and V. K. Lazarov, NPG Asia Materials **9**, e402 (2017).

[62] P.-C. Yeh, W. Jin, N. Zaki, D. Zhang, J. T. Sadowski, A. Al-Mahboob, A. M. van der Zande, D. A. Chenet, J. I. Dadap, I. P. Herman, P. Sutter, J. Hone, and R. M. Osgood, Phys. Rev. B **89**, 155408 (2014).

[63] B. Das, S. Maity, S. Paul, K. Dolui, S. Paramanik, S. Naskar, S. R. Mohanty, S. Chakraborty, A. Ghosh, M. Palit, *et al.*, ACS nano **15**, 20203 (2021).

[64] K. Shahil, M. Hossain, V. Goyal, and A. Balandin, Journal of Applied Physics **111** (2012).

[65] K. Shahil, M. Hossain, D. Teweldebrhan, and A. Balandin, Applied physics letters **96** (2010).

[66] J.-U. Lee, S. Lee, J. H. Ryoo, S. Kang, T. Y. Kim, P. Kim, C.-H. Park, J.-G. Park, and H. Cheong, Nano letters **16**, 7433 (2016).

[67] D. Dey, A. Ray, and L. Yu, Phys. Rev. Mater. **6**, L061002 (2022).

[68] K. Zollner, M. Gmitra, T. Frank, and J. Fabian, Phys. Rev. B **94**, 155441 (2016).

[69] J. B. Goodenough, Phys. Rev. **100**, 564 (1955).

[70] J. Kanamori, Journal of Physics and Chemistry of Solids **10**, 87 (1959).

[71] A. Smolyanitsky and V. K. Tewary, Nanotechnology **22**, 085703 (2011).

[72] C. Zhang, M.-Y. Li, J. Tersoff, Y. Han, Y. Su, L.-J. Li, D. A. Muller, and C.-K. Shih, Nature nanotechnology **13**, 152 (2018).

[73] G. Rosenberg and M. Franz, Phys. Rev. B **85**, 195119 (2012).

[74] D. Dey, T. Maitra, U. Waghmare, and A. Taraphder, Physical Review B **101**, 205132 (2020).

[75] P. E. Bl, Physical Review B **50**, 953 (1994).

[76] G. Kresse and D. Joubert, Physical review b **59**, 1758 (1999).

[77] G. Kresse and J. Furthmüller, Phys. Rev. B **54**, 11169 (1996).

[78] G. Kresse and J. Furthmüller, Computational materials science **6**, 15 (1996).

[79] J. P. Perdew, K. Burke, and M. Ernzerhof, Physical review letters **77**, 3865 (1996).

[80] S. L. Dudarev, G. A. Botton, S. Y. Savrasov, C. Humphreys, and A. P. Sutton, Physical Review B **57**, 1505 (1998).

[81] Y. Zheng, X.-x. Jiang, X.-x. Xue, J. Dai, and Y. Feng, Phys. Rev. B **100**, 174102 (2019).

[82] B. L. Chittari, Y. Park, D. Lee, M. Han, A. H. MacDonald, E. Hwang, and J. Jung, Phys. Rev. B **94**, 184428 (2016).

[83] D. Dey, T. Maitra, and A. Taraphder, Physical Review B **93**, 195133 (2016).

[84] S. Baroni, S. De Gironcoli, A. Dal Corso, and P. Giannozzi, Reviews of modern Physics **73**, 515 (2001).

[85] A. Togo and I. Tanaka, Scripta Materialia **108**, 1 (2015).

[86] S. Smidstrup, T. Markussen, P. Vancraeyveld, J. Wellendorff, J. Schneider, T. Gunst, B. Verstichel, D. Stradi, P. A. Khomyakov, U. G. Vej-Hansen, *et al.*, Journal of Physics: Condensed Matter **32**, 015901 (2019).

[87] D. Stradi, L. Jelver, S. Smidstrup, and K. Stokbro, Journal of Physics: Condensed Matter **29**, 185901

(2017).

[88] S. Grimme, J. Antony, S. Ehrlich, and H. Krieg, The Journal of chemical physics **132**, 154104 (2010).

[89] M. Pajda, J. Kudrnovský, I. Turek, V. Drchal, and P. Bruno, Phys. Rev. B **64**, 174402 (2001).

[90] J. P. Perdew, K. Burke, and M. Ernzerhof, Phys. Rev. Lett. **77**, 3865 (1996).

[91] M. van Setten, M. Giantomassi, E. Bousquet, M. Verstraete, D. Hamann, X. Gonze, and G.-M. Rignanese, Computer Physics Communications **226**, 39 (2018).

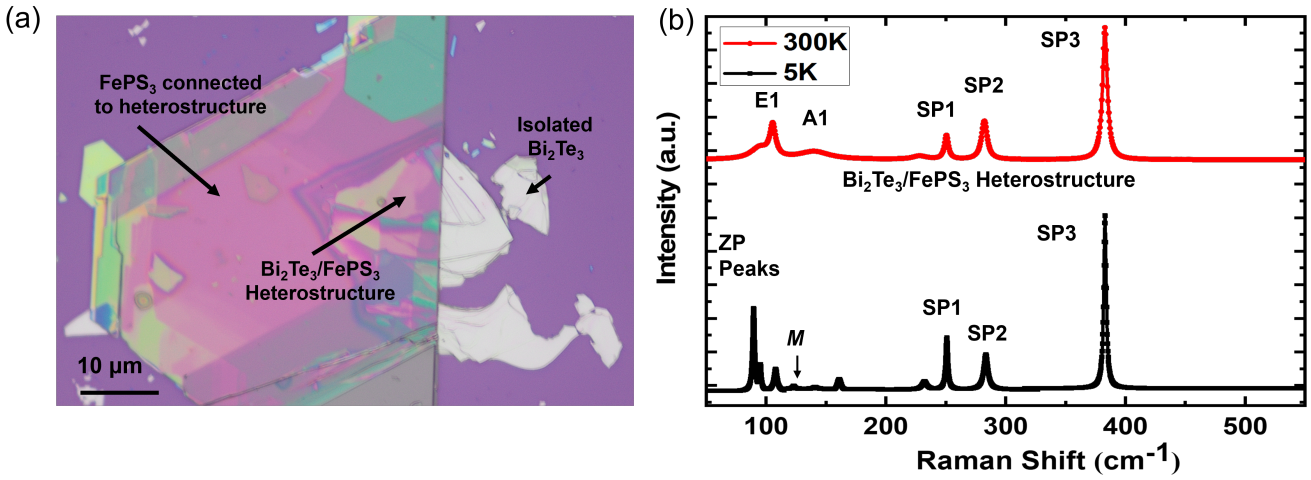

FIG. 1. (a) Optical microscopy image of heterostructure (HS-1) fabricated *via* stamping method onto a 300 nm Si/SiO_2 substrate. Raman spectroscopy of (b) $Bi_2Te_3/FePS_3$ heterostructure (HS-1) at 5 K and room temperature obtained with an excitation wavelength 473 nm. Spin-phonon coupled peaks and Magnon Peak are designated as SP(1-3) and M respectively. Zone folded phonon modes (ZPs) appear at low temperature is not present at room temperature. Individual characteristics phonon modes of Bi_2Te_3 (denoted as E1 and A1) and $FePS_3$ are present in $Bi_2Te_3/FePS_3$ heterostructure.

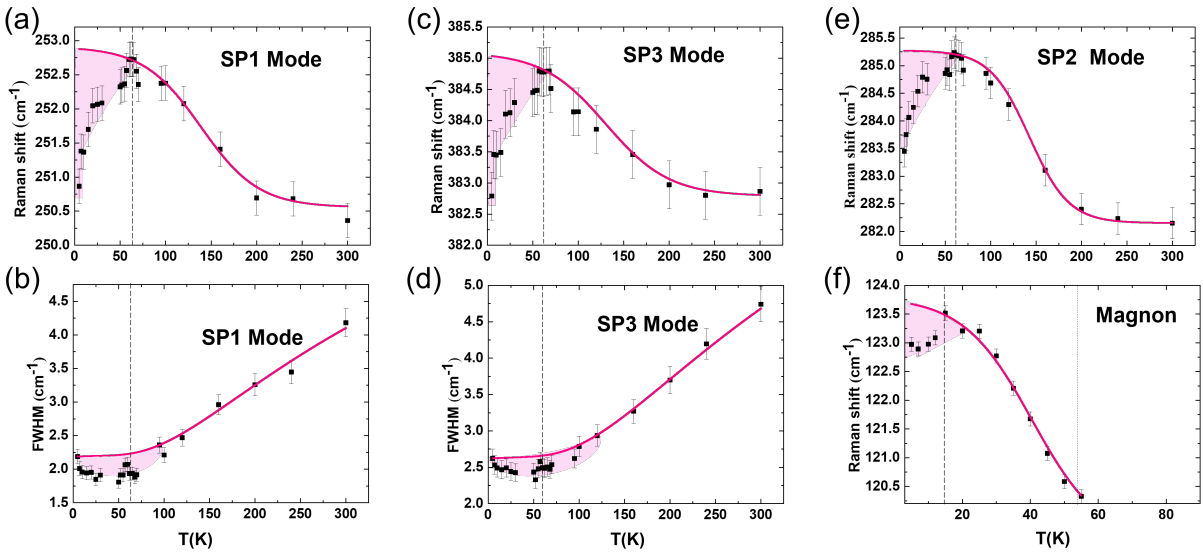

FIG. 2. Variation of Peak position and linewidth of $FePS_3$ Raman modes (a), (b) SP1 mode; (c), (d) SP3 mode; (e) SP2 mode (f) Magnon mode in the heterostructure (HS-1) with temperature. All spin-phonon peaks show phonon anomaly at around 65 K in phonon frequency. At below 65 K, linewidths of all spin-phonon mode of $FePS_3$ are not fit with 3-phonon Anharmonic Decay (AD) model due to presence of Bi_2Te_3 underneath. One-magnon mode [Fig.(f)] at 120 cm^{-1} at a temperature ($T_M \sim 60$ K) was observed in $FePS_3$. Softening of this magnon mode was observed with the temperature and the softening temperature becomes half due to Bi_2Te_3 underneath.

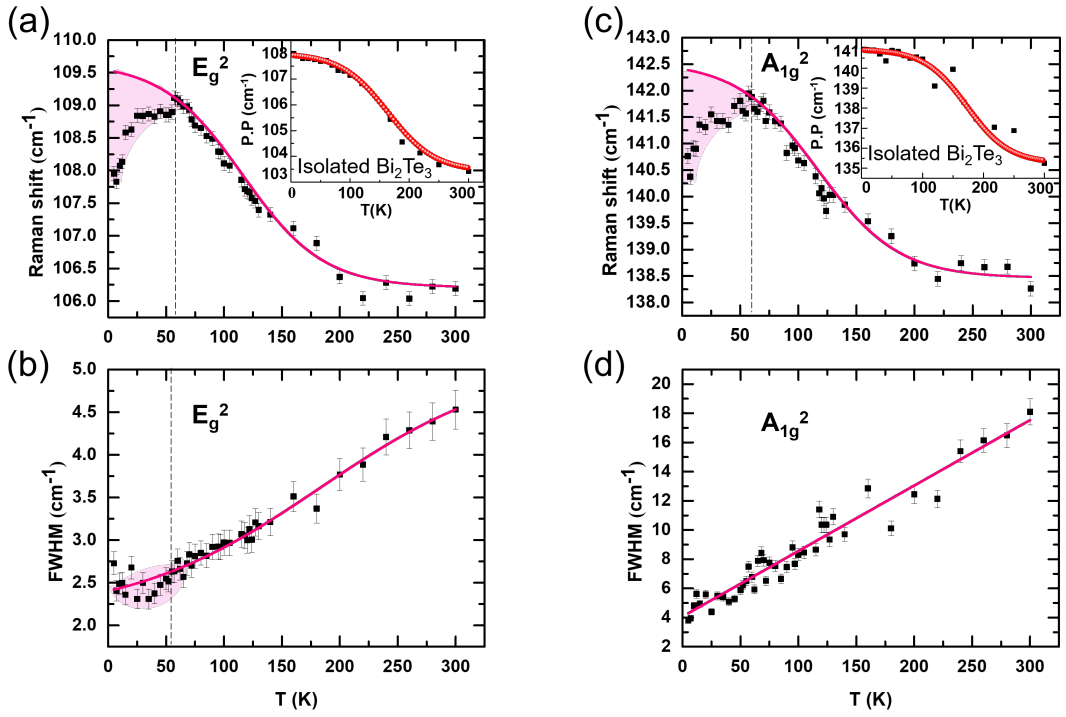

FIG. 3. Variation of peak position and linewidth of Raman modes of Bi_2Te_3 in the heterostructure (HS-1) (a),(b) In-plane Raman mode E_g^2 ; (c),(d) Out-of-plane Raman mode A_{1g}^2 of Bi_2Te_3 with temperature. Insets (a), (c) showing the temperature dependence of Raman modes of isolated Bi_2Te_3. No phonon anomaly was observed in the in-plane and out-of-plane Raman modes of isolated Bi_2Te_3. In case of Bi_2Te_3 in the heterostructure (HS-1), phonon anomaly was observed in both Raman modes of Bi_2Te_3 in phonon frequency at around 60 K. Linewidth of in-plane Raman mode [Fig (b)] of Bi_2Te_3 was not fit by Boltzmann sigmoidal anharmonic curve at/below 60 K. Linewidth of out-of-plane Raman mode of Bi_2Te_3 [Fig(d)] increases with the temperature in the whole temperature window.

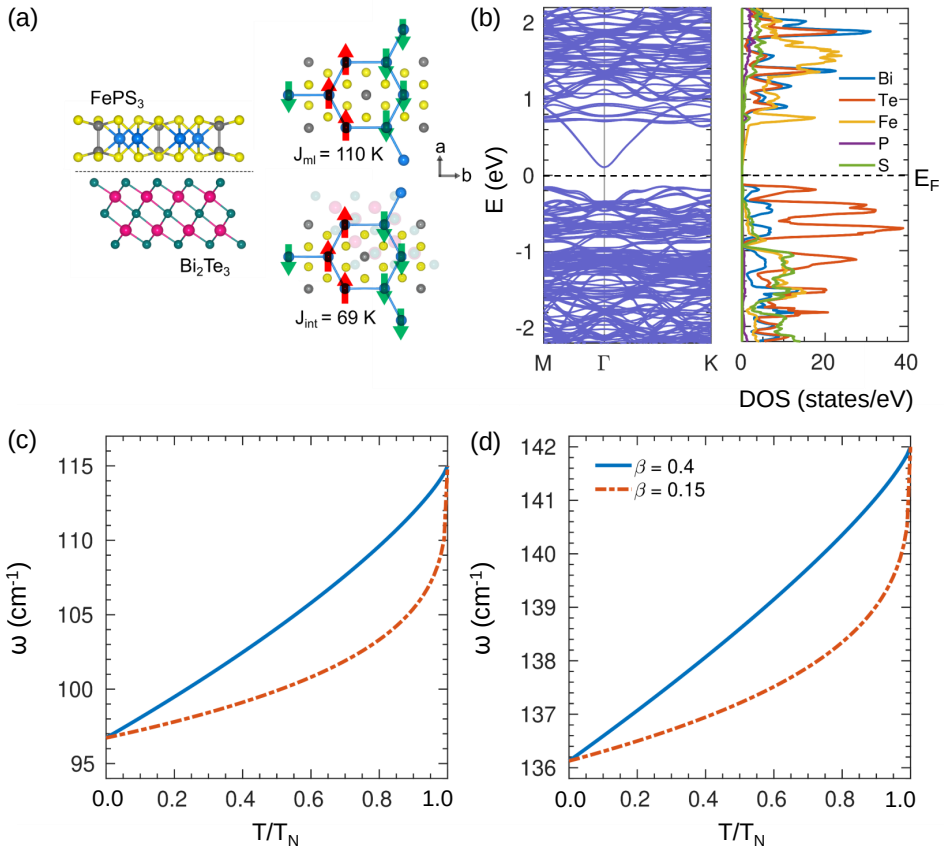

FIG. 4. (a) A schematic of Bi_2Te_3/$FePS_3$ heterostructure and the zigzag AFM order of an isolated $FePS_3$ monolayer and a monolayer on top of Bi_2Te_3. The respective AFM exchange values are also shown. (b) Band structure and atom projected density of states (DOS) of Bi_2Te_3/$FePS_3$ heterostructure obtained within GGA+U+SOC reveal that the system is a narrow band gap semiconductor. Temperature dependence of (c) 115 cm^{-1} and (d) 141 cm^{-1} $FePS_3$ phonon modes that are coupled to Bi_2Te_3 modes are shown for two critical exponent (β) values obtained from experiments.

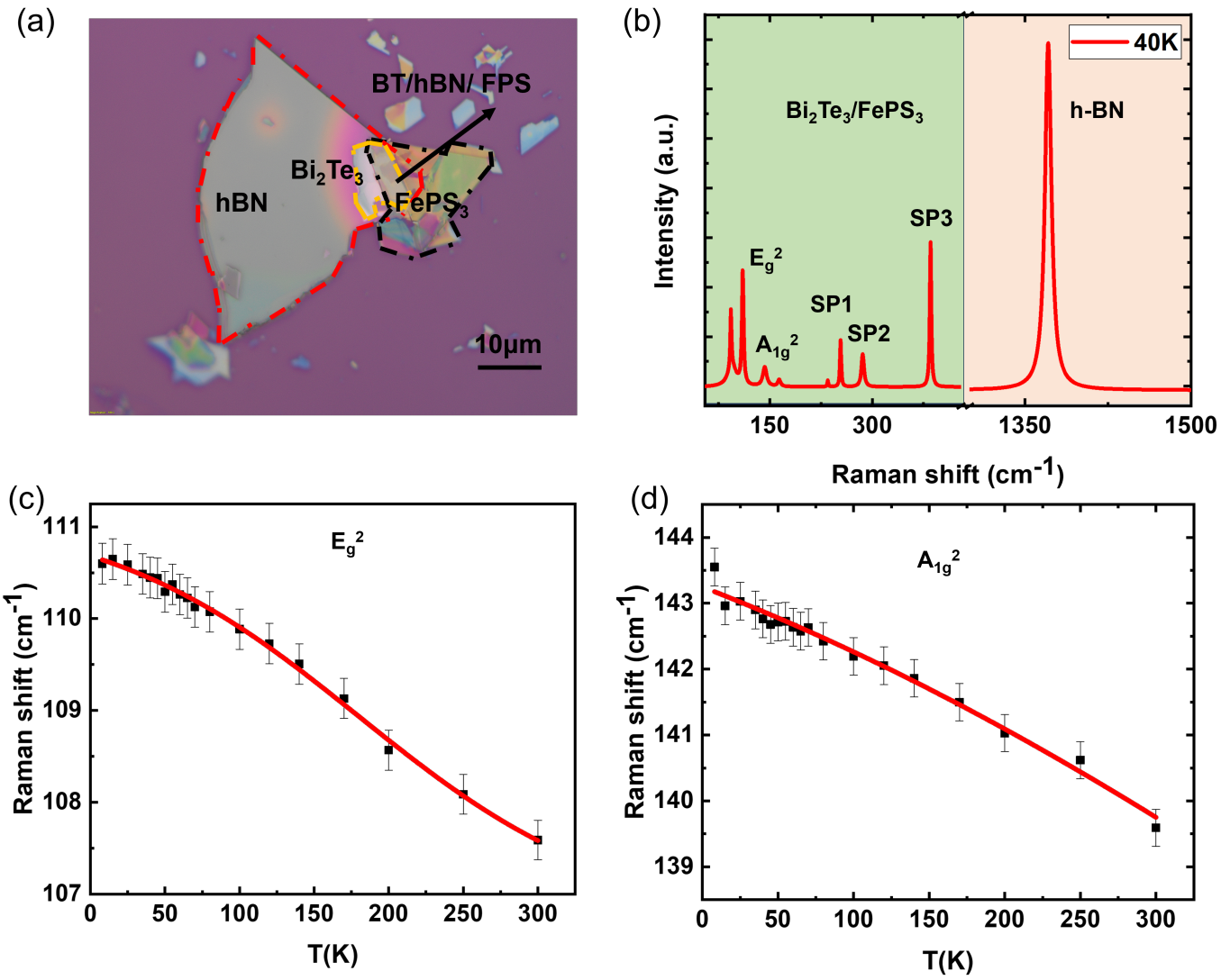

FIG. 5. (a) Optical microscopy image of heterostructure (HS-4). Orange dotted line surrounds Bi_2Te_3 flake. Bulk hBN (red dotted line) is first placed on top of Bi_2Te_3. $FePS_3$ (black dotted line) covers both Bi_2Te_3 (some portion) and hBN (some portion) resulting the formation of Bi_2Te_3/hBN/ $FePS_3$ heterostructure. (b) Raman spectra of the heterostructure (HS-4) at low temperature. Individual Raman modes of Bi_2Te_3, hBN and $FePS_3$ are appeared in Bi_2Te_3/hBN/ $FePS_3$ heterostructure . Variation of peak position of Raman modes of Bi_2Te_3 (c) In-plane Raman mode E_g^2 ; (d) Out-of-plane Raman mode A_{1g}^2 of Bi_2Te_3 with temperature in the heterostructure (figure (a)). No phonon anomaly was observed in the in-plane and out-of-plane Raman modes of Bi_2Te_3 due to the presence of hBN like isolated one.

Supplementary Information: Manipulating Spin-Lattice Coupling in Layered Magnetic Topological Insulator Heterostructure *via* Interface Engineering

Sujan Maity,[1] Dibyendu Dey,[2] Anudeepa Ghosh,[1] Suvadip Masanta,[3] Binoy Krishna De,[4] Hemant Singh Kunwar,[4] Bikash Das,[1] Tanima Kundu,[1] Mainak Palit,[1] Satyabrata Bera,[1] Kapildeb Dolui,[5] Kenji Watanabe,[6] Takashi Taniguchi,[7] Liping Yu,[2] A Taraphder,[8] and Subhadeep Datta*[1]

[1]*School of Physical Sciences, Indian Association for the Cultivation of Science, 2A & 2B Raja S. C. Mullick Road, Jadavpur, Kolkata - 700032, India*

[2]*Department of Physics and Astronomy, University of Maine, Orono, ME 04469, USA*

[3]*Bose Institute, Department of Physics Main Campus 93/1, A. P. C. Road Kolkata - 700 009, India*

[4]*UGC-DAE Consortium for Scientific Research, Indore Centre, University Campus, Khandwa Road, Indore 452001*

[5]*Lomare Technolgies Limited, 6 London Street, London EC3R 7LP, United Kingdom*

[6]*Research Center for Functional Materials, National Institute for Materials Science, Tsukuba 305-0044, Japan*

[7]*International Center for Materials Nanoarchitectonics, National Institute for Materials Science,Tsukuba 305-0044, Japan*

[8]*Department of Physics, Indian Institute of Technology Kharagpur, W.B. 721302, India*

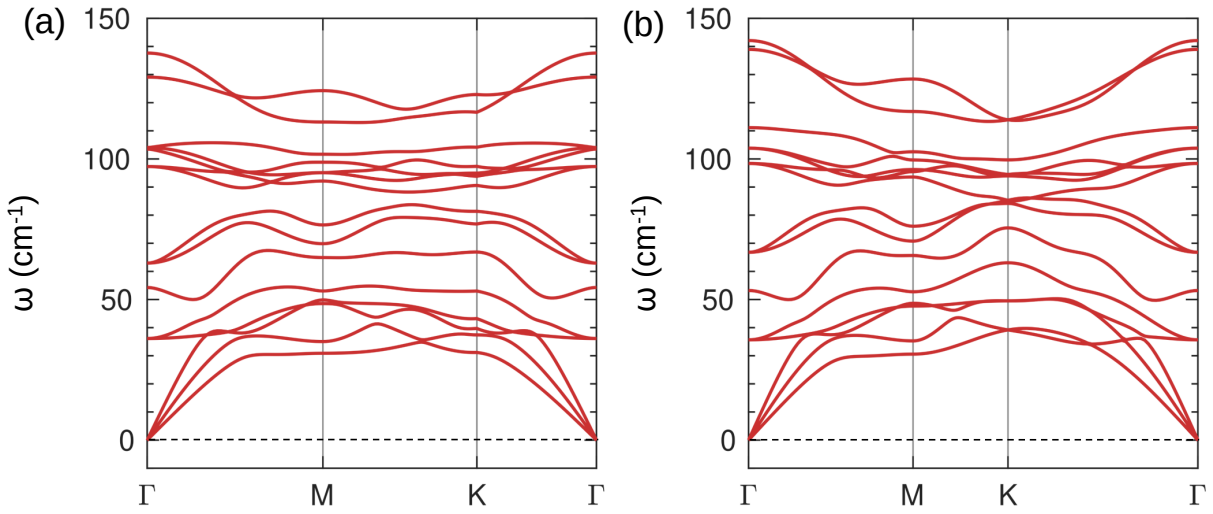

FIG. S1. Phonon dispersion of Bi_2Te_3 (a) bulk and (b) monolayer structures, respectively. The phonon dispersion of Bi_2Te_3 monolayer agree well with its bulk counterpart. No imaginary frequencies have been observed in phonon dispersion, suggesting that this structure is dynamically stable.

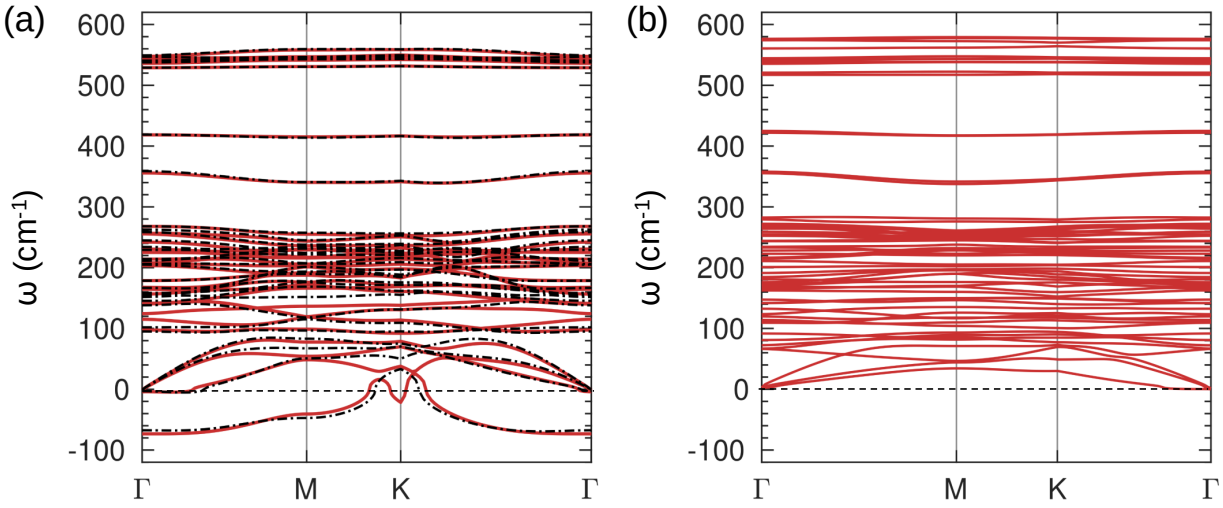

FIG. S2. (a) Phonon dispersion of $FePS_3$ monolayer for z-AFM (red solid lines) and FM (black dotted lines) spin configurations in the experimentally reported point-group structure. (b) Phonon dispersion of distorted $FePS_3$ monolayer for z-AFM spin configuration indicate the dynamical stability due to the absence of imaginary modes

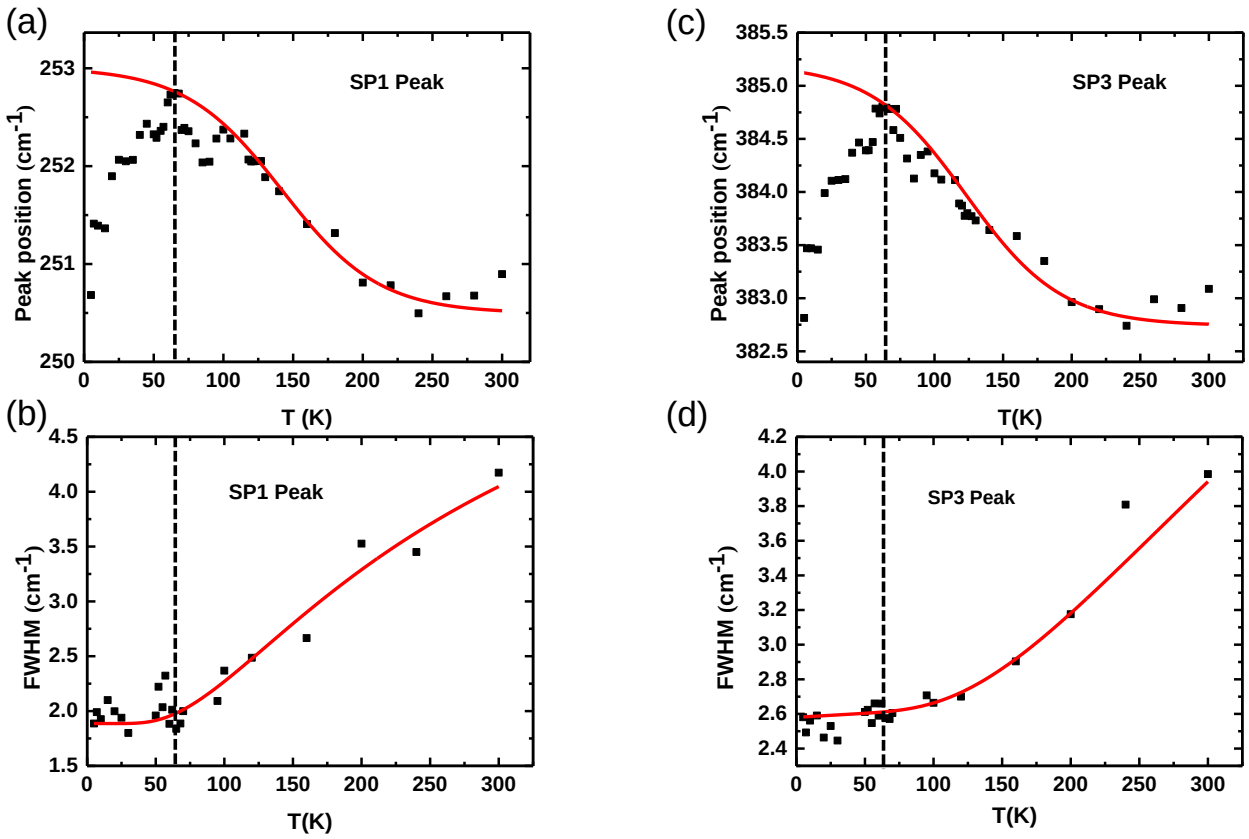

FIG. S3. Variation of Peak position and linewidth of $FePS_3$ Raman modes connected to heterostructure with temperature. (a),(b) SP1 mode; (c), (d) SP3 mode; All spin-phonon peaks show phonon anomaly at around 65 K in phonon frequency. Linewidths of all spin-phonon mode of $FePS_3$ are fit with 3-phonon anharmonic decay (AD) model.

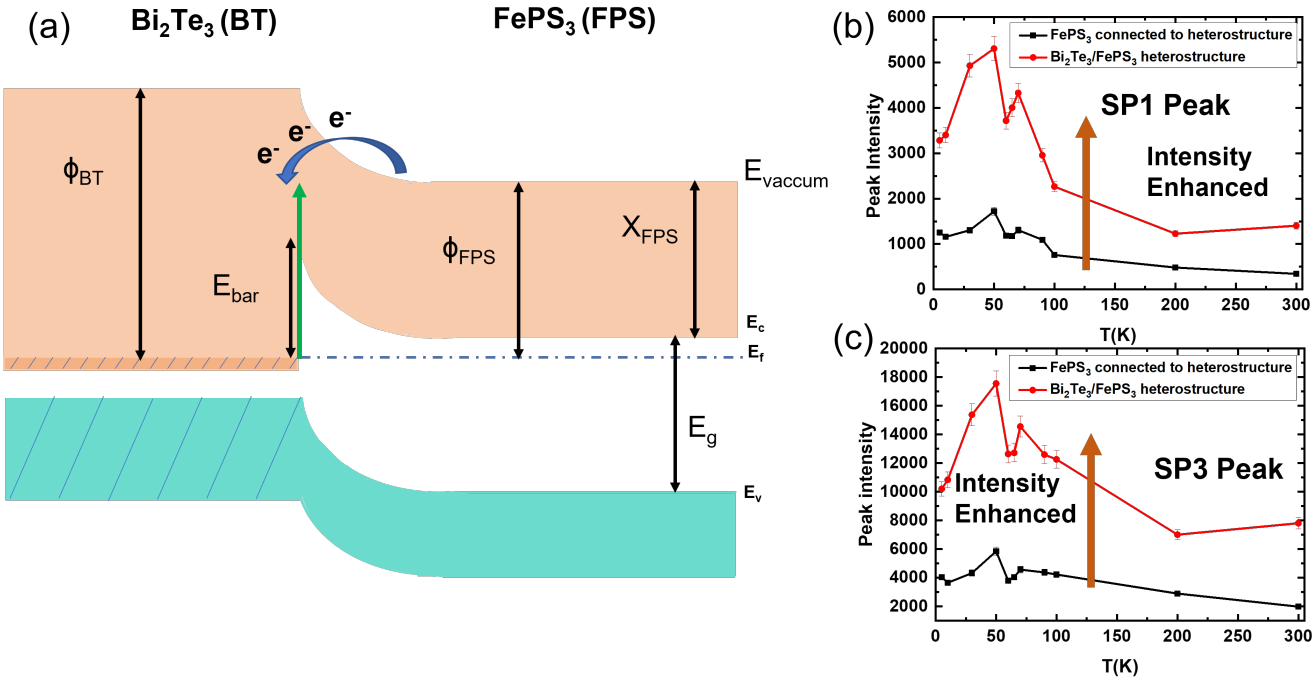

FIG. S4. (a) Schematic diagram of the band bending that occurs at the interface between the metallic Bi_2Te_3 and the semiconducting $FePS_3$. The work function of Bi_2Te_3 ($\phi_{Bi_2Te_3}$ = 5.30 eV) is larger than that of $FePS_3$ (ϕ_{FePS_3} = 4.23 eV) which leads to the formation of a Schottky barrier of height $\phi_{Bi_2Te_3}$ - χ_{FePS_3} = 1.17 eV at the interface. To balance out the chemical potential electrons move from the $FePS_3$ into the Bi_2Te_3. (b), (c) Intensity of Raman peaks of $FePS_3$ are enhanced due to Bi_2Te_3 underneath compare to isolated $FePS_3$ Raman modes. In Bi_2Te_3-$FePS_3$ heterostructure, barrier height (E_{bar}) (1.17 eV)< Raman excitation (denoted by green arrow) (2.62 eV). The available transitions for Raman scattering will then involve real energy levels, drastically enhancing the intensity

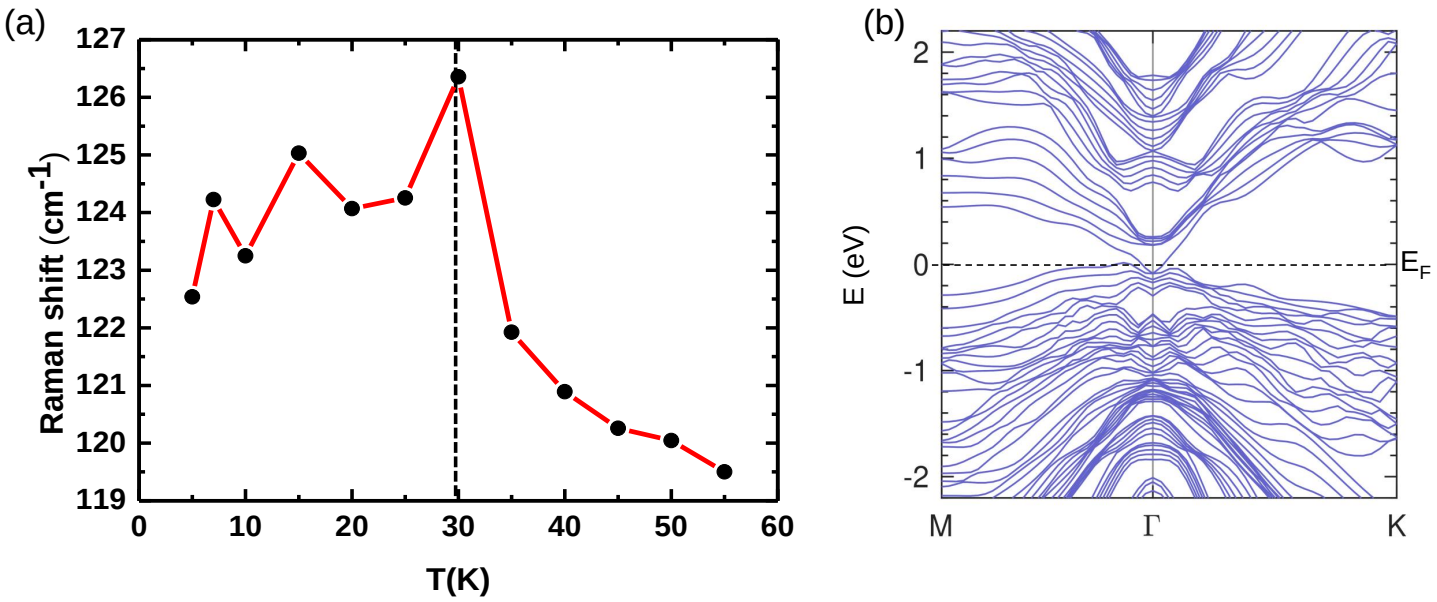

FIG. S5. (a) Magnon mode of $FePS_3$ connected to heterostructure. One-magnon mode at 120 cm^{-1} at a temperature ($T_M \sim 60K$) was observed in $FePS_3$. Softening of this magnon mode was observed with the temperature and the softening temperature is 30K in case of $FePS_3$. (b) Electronic structure of 6 quintuple layers of Bi_2Te_3. Metallic surface states start appearing at a thickness ($\sim$ 6 nm) of 6 quintuple layers.

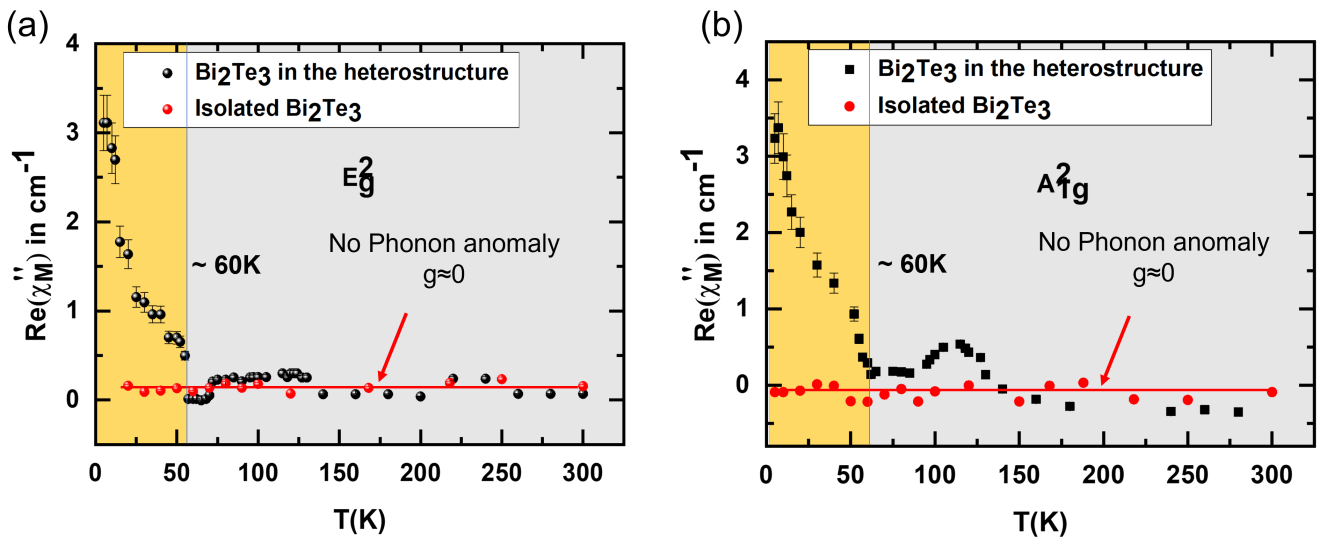

FIG. S6. Real part of Magnetic Susceptibility of (a) In-plane E_g^2 mode; (b) Out-of-plane A_{1g}^2 mode of Bi_2Te_3 in $Bi_2Te_3/FePS_3$ heterostructure ; No such change in spin-phonon coupling constant (g) was observed with temperature in both Raman modes of isolated Bi_2Te_3 due to pure phononic behaviour in the whole temperature range. In case of Bi_2Te_3, in the heterostructure, slope of the curve changes around 60K and this is the reflection of proximity induced spin-phonon coupling of Bi_2Te_3 , occurs at/around 60K.

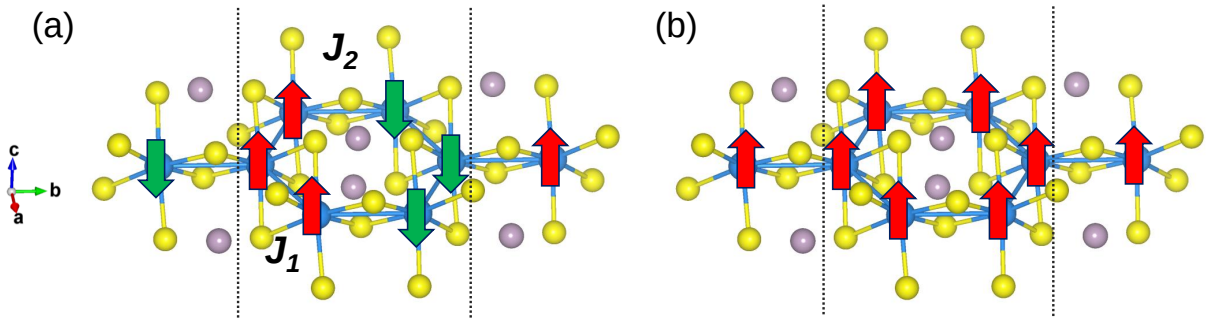

FIG. S7. (a) zig-zag AFM and (b) FM spin configurations of $FePS_3$ monolayer that are used to evaluate Fe-Fe AFM exchange.

By mapping the DFT total energy of z-AFM (E_1) and FM spin configurations (E_2) to the Heisenberg spin model, $H = J \sum_{i>j} S_i \cdot S_j$, we obtain the following equations-

$$E_1 = 4J_1S^2 - 2J_2S^2 + \epsilon \tag{1}$$

$$E_2 = 4J_1S^2 + 2J_2S^2 + \epsilon \tag{2}$$

$$J_2 = \frac{(E_2 - E_1)}{4S^2} \tag{3}$$

where, J_1 is the FM exchange along the a-axis and J_2 is the AFM exchange along the b-axis. Stronger J_2 indicates higher T_N, whereas weaker J_2 indicates lower T_N.

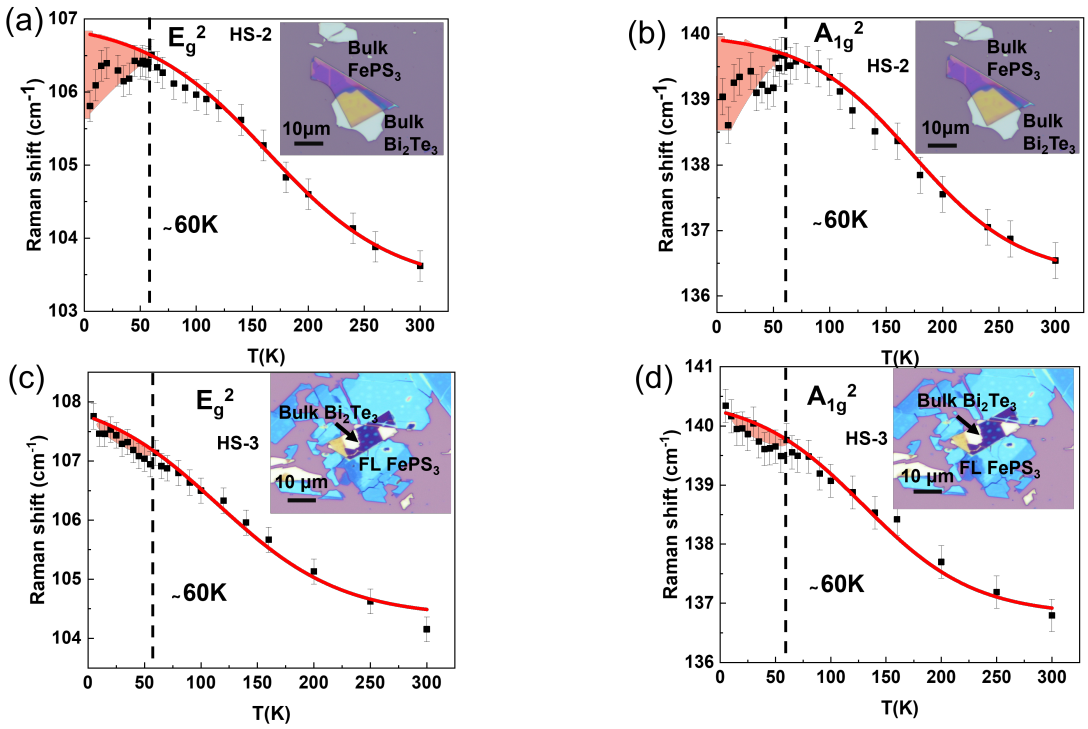

FIG. S8. Thickness dependent Raman studies on Bi_2Te_3/$FePS_3$ heterostructure with temperature.(a) In-plane phonon mode (E_g^2) and (b) Out-of-plane phonon mode (A_{1g}^2) of Bi_2Te_3 in bulk Bi_2Te_3 / bulk $FePS_3$ heterostructure (HS-2) and, (c) In-plane phonon mode (E_g^2) and (d) Out-of-plane phonon mode (A_{1g}^2) of Bi_2Te_3 in bulk Bi_2Te_3/Few layer $FePS_3$ heterostructure (HS-3). Insets are showing the optical microscopy images of HS-2 and HS-3. The deviation from anharmonic behaviour, $\Delta\omega$ (related to square of magnetization) values for HS-2 and HS-3 heterostructures, are 0.69 and 0.57 respectively for both phonon modes of Bi_2Te_3. Strength of the spin-phonon coupling decreases but phonon anomaly in both Raman modes of Bi_2Te_3 remains invariant ($\sim$ 60K) with reduction of thickness of the heterostructures.

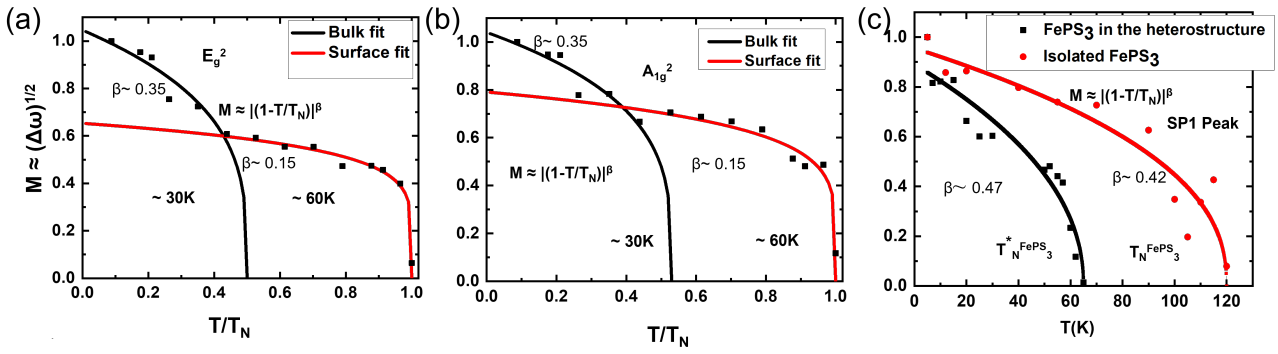

FIG. S9. Antiferromagnetic order parameter of (a) In plane E_g^2 mode; (b) out of plane A_{1g}^2 mode of Bi_2Te_3 in the heterostructure ; (c) SP1 peak for two different configurations, $FePS_3$ in the heterostructure (T_N^*) and isolated $FePS_3$ (T_N) respectively as a function of temperature. Data points are fit with $M \approx |(1 - \frac{T}{T_N})|^\beta$ equation. β is the critical exponent. The β value at 60K (0.15) for surface magnetism corroborates the value of 2D Ising model. The β value at 30K (0.35) corresponds to 3D Heisenberg model, responsible for bulk contribution. The β values for the $FePS_3$ [Fig (c)] are close to mean field value.

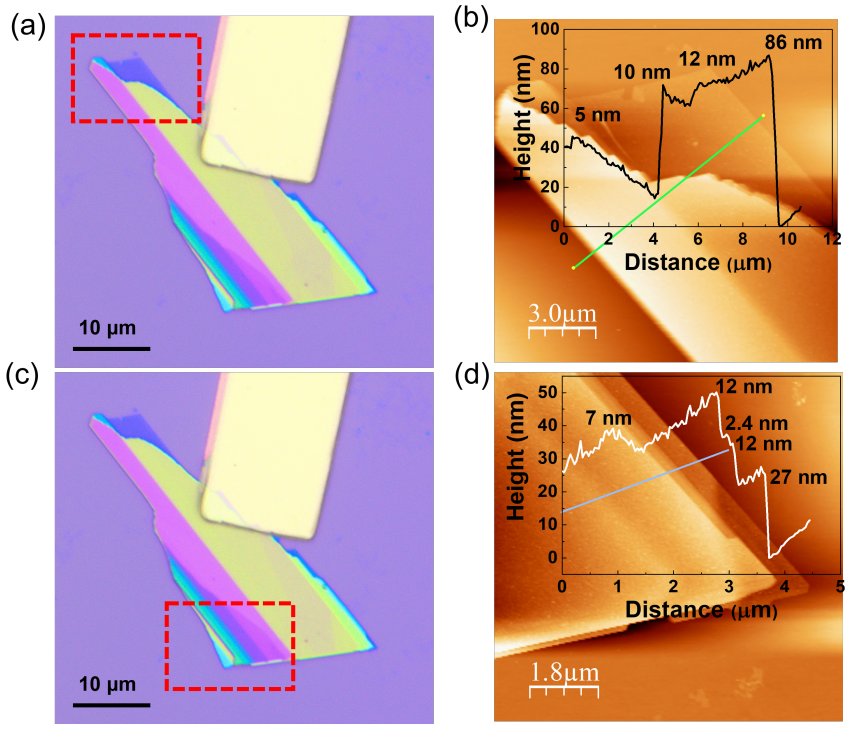

FIG. S10. (a), (c) Optical microscopy image of $FePS_3$ flake 1. (b), (d) Atomic force microscopy images of the highlighted area of the flake 1. Insets of (b), (d) show the height profile of the flake.

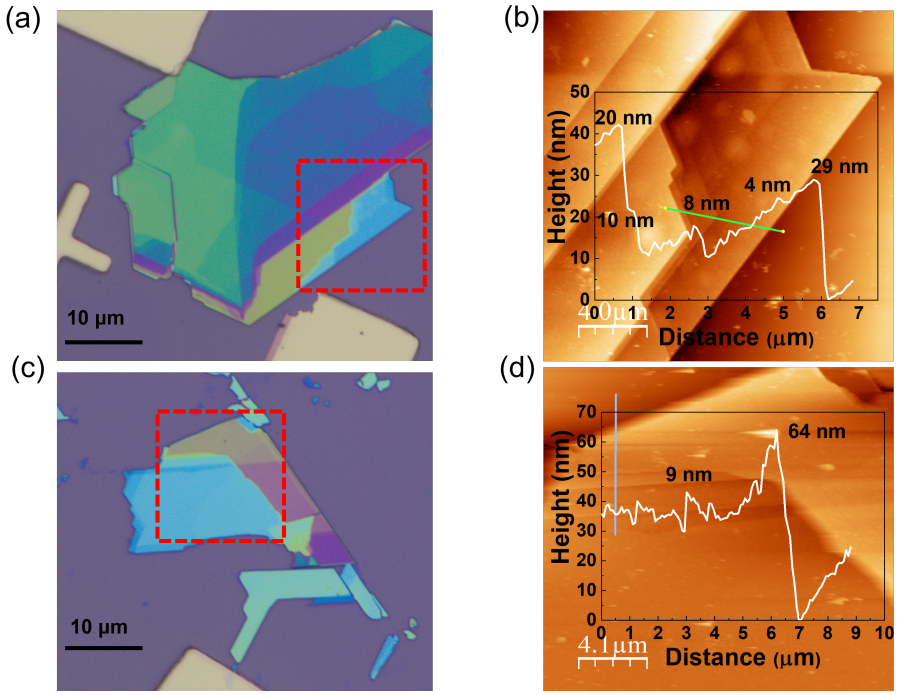

FIG. S11. (a), (c) Optical microscopy image of $FePS_3$ flake 2 and flake 3. (b), (d) Atomic force microscopy images of the highlighted area of the flake 2 and 3. Insets of (b), (d) show the height profile of the flakes.

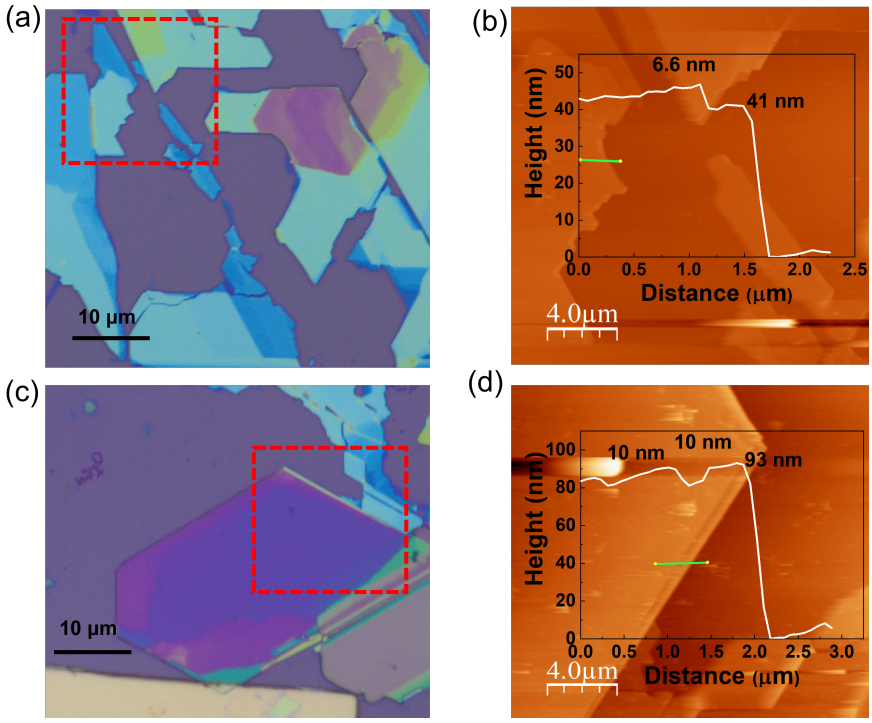

FIG. S12. (a), (c) Optical microscopy image of $FePS_3$ flake 4 and flake 5. (b), (d) Atomic force microscopy images of the highlighted area of the flake 4 and flake 5. Insets of (b), (d) show the height profile of the flakes.

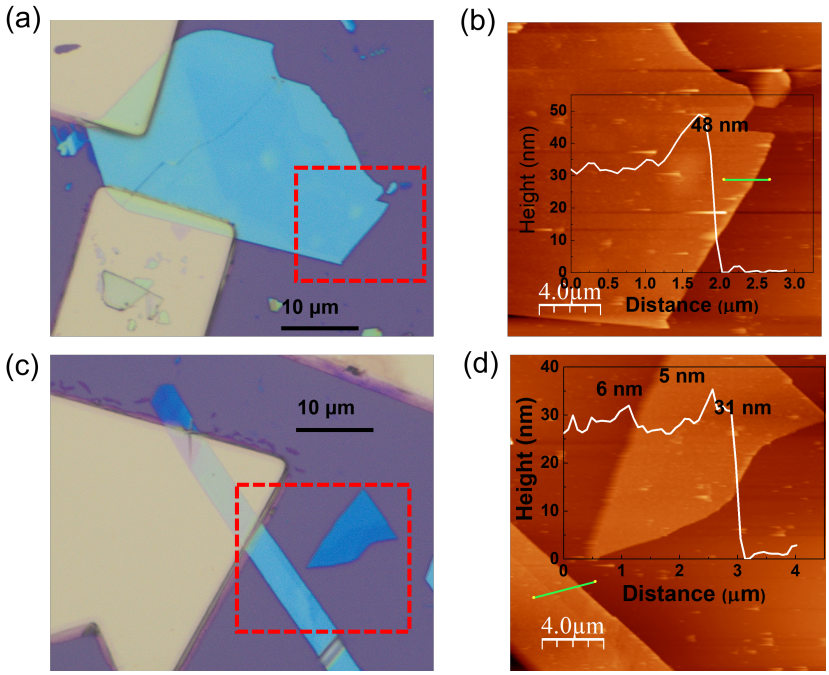

FIG. S13. (a), (c) Optical microscopy image of $FePS_3$ flake 6 and flake 7. (b), (d) Atomic force microscopy images of the highlighted area of the flake 6 and flake 7. Insets of (b), (d) show the height profile of the flakes.

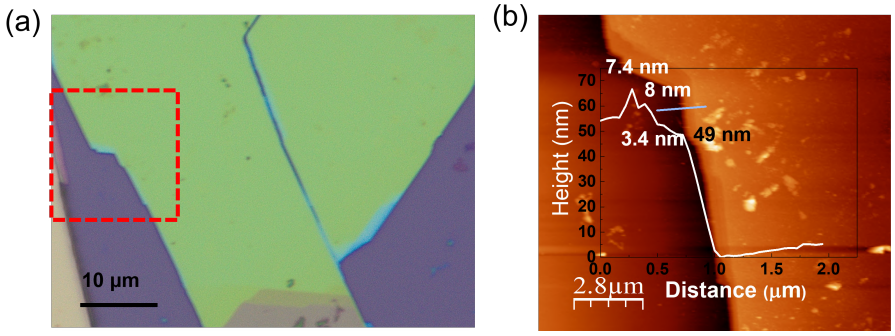

FIG. S14. (a) Optical microscopy image of $FePS_3$ flake 8. (b) Atomic force microscopy image of the highlighted area of the flake 8. Inset of (b) shows the height profile of the flake.

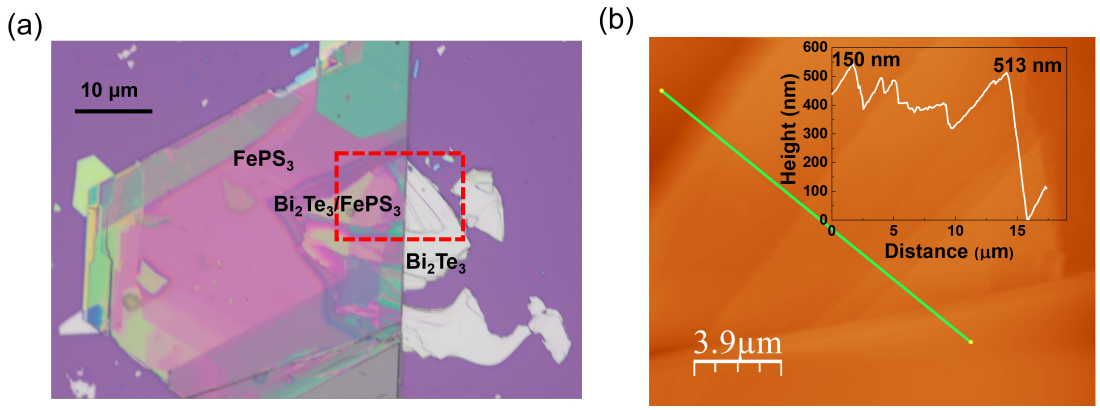

FIG. S15. (a) Optical microscopy image of $Bi_2Te_3/FePS_3$ heterostructure (HS-1). (b) Atomic force microscopy image of $Bi_2Te_3/FePS_3$ (HS-1). Inset of (b) shows the height profile of the heterostructure.

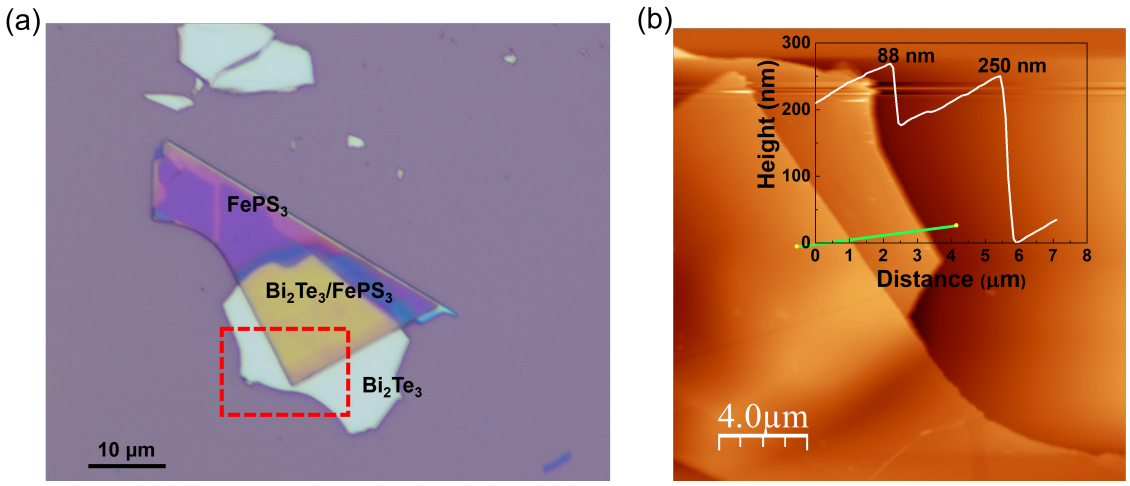

FIG. S16. (a) Optical microscopy image of $Bi_2Te_3/FePS_3$ (HS-2). (b) Atomic force microscopy image of $Bi_2Te_3/FePS_3$ (HS-2). Inset of (b) shows the height profile of the heterostructure.

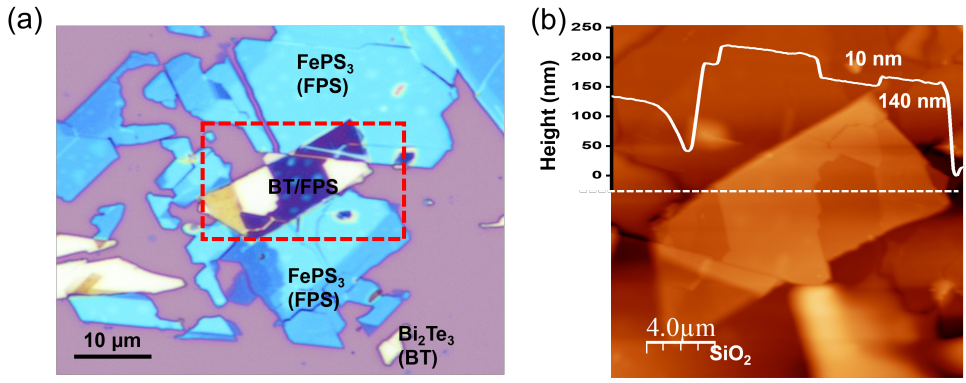

FIG. S17. (a) Optical microscopy image of Bi_2Te_3/$FePS_3$ (HS-3). (b) Atomic force microscopy image of Bi_2Te_3/$FePS_3$ (HS-3). Inset of (b) shows the height profile of the heterostructure.

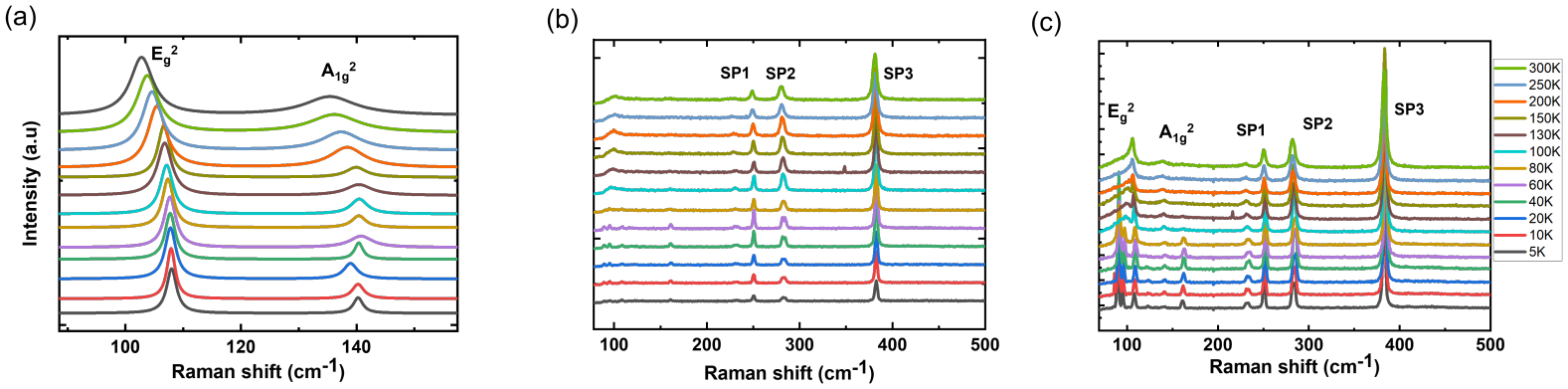

FIG. S18. Raman spectra of (a) isolated Bi_2Te_3, (b) isolated $FePS_3$, (c) Bi_2Te_3/$FePS_3$ heterojunction of multiple sampling points at different temperature (5K to 300K)

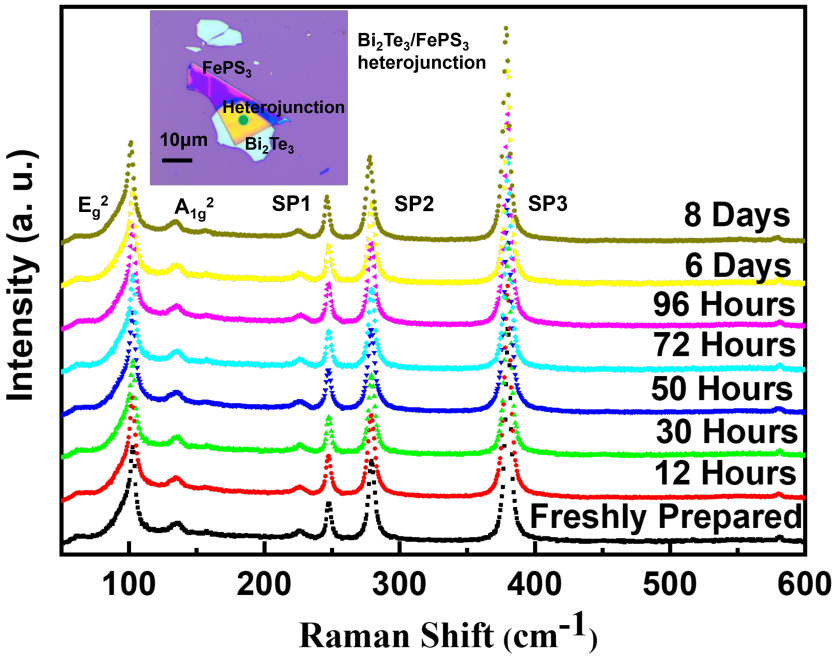

FIG. S19. Raman Spectra of $Bi_2Te_3/FePS_3$ heterojunction were recorded for 8 days to check the air stability of the heterostructure. Inset shows the optical microscopy image of the heterostructure. Green dot in heterojunction signifies the laser spot. No change was observed in peak position and linewidth of Bi_2Te_3 and $FePS_3$ Raman modes.

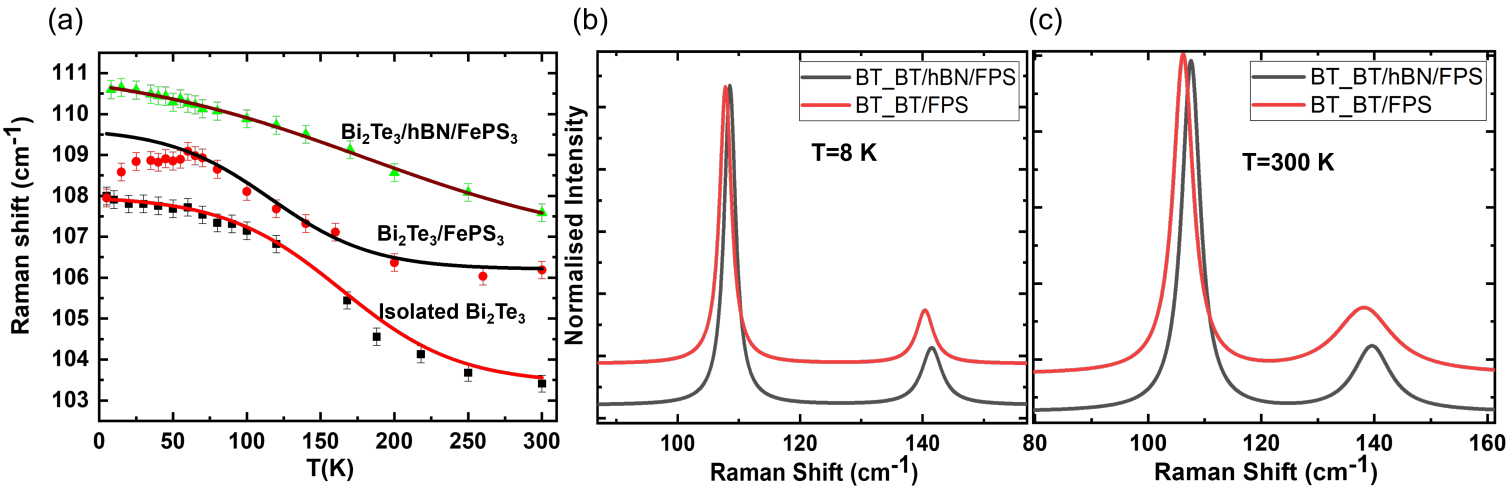

FIG. S20. (a) Variation of in-plane Raman modes of Bi_2Te_3 are plotted with temperature for isolated and for different heterostructures; (b), (c) Raman shifts of Bi_2Te_3 modes are shown for two different temperatures in heterostructures.

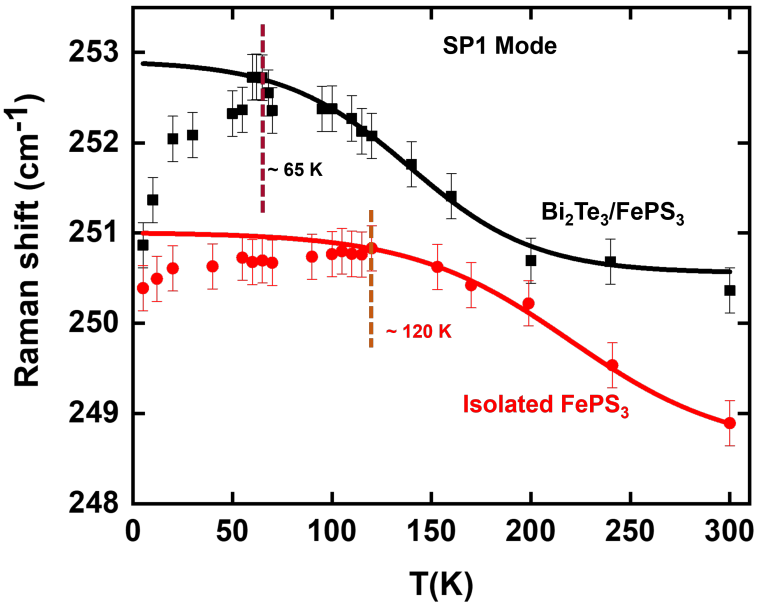

FIG. S21. Variation of $FePS_3$ spin-phonon coupled mode (SP1) with temperature for two different configurations. In case of isolated $FePS_3$, the characteristic Néel temperature (T_N) is around 120 K and reduction of T_N was observed at/around 65 K due to Bi_2Te_3 underneath in heterostructure.

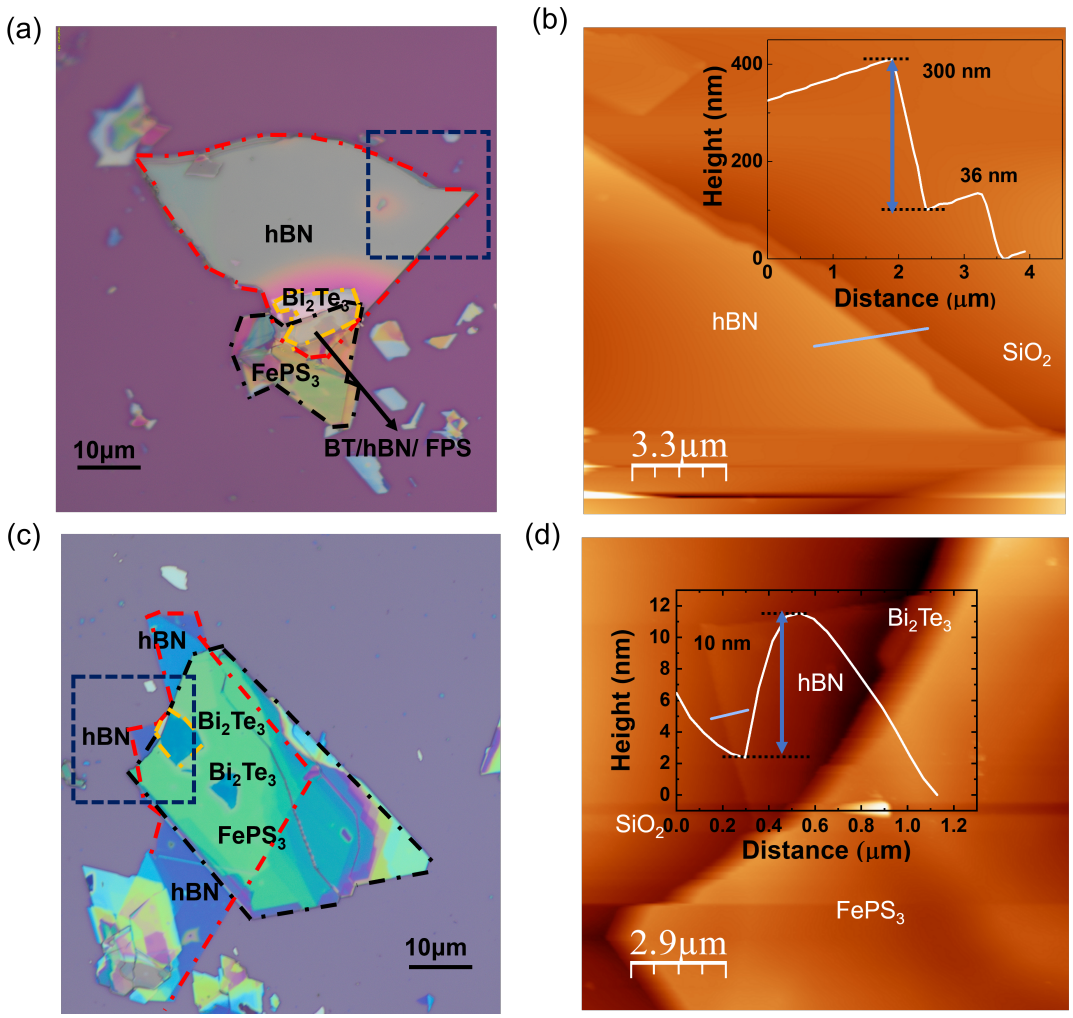

FIG. S22. (a), (c) Optical microscopy images of Bi_2Te_3/hBN/$FePS_3$ HS with two different thickness of hBN. (b),(d) Atomic force microscopy images of HS. Insets of (b), (d) show the height profile of hBN

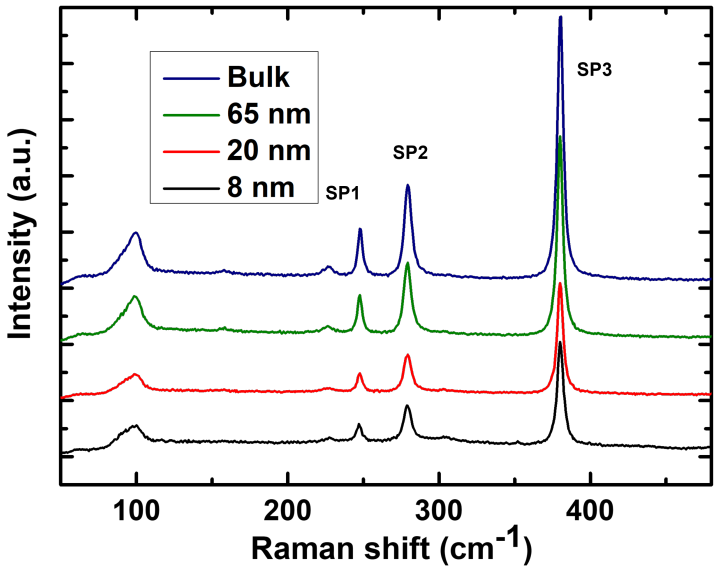

FIG. S23. Room temperature Raman spectra of $FePS_3$ with varying thickness. No significant Raman shift was observed with thickness indicating layer dependent stability of vibrational modes even in few layer $FePS_3$.

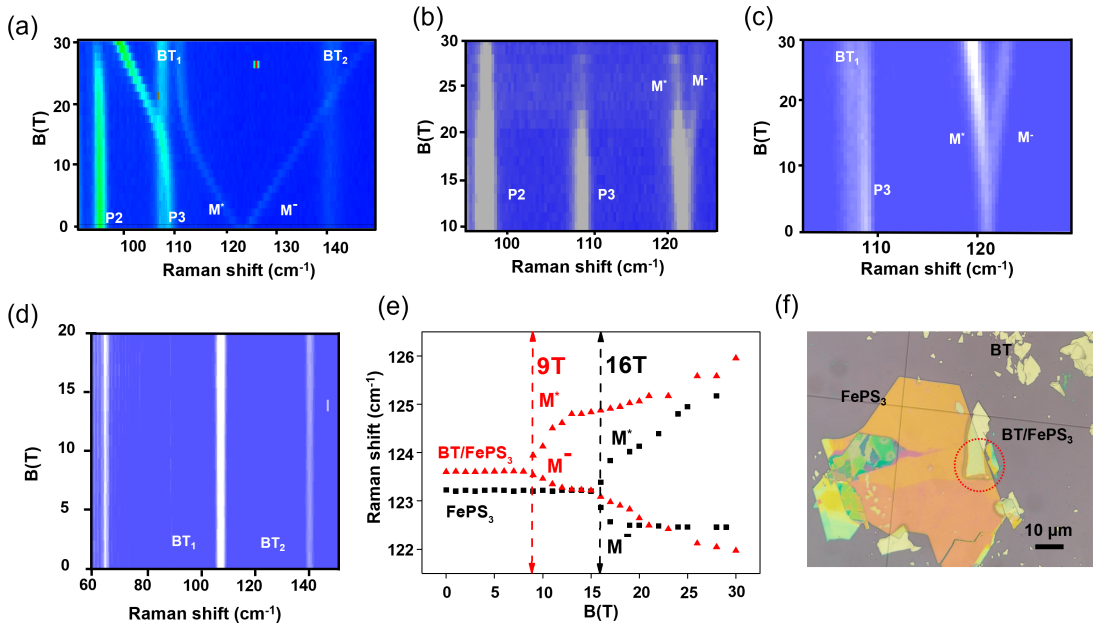

FIG. S24. (a) Evolution of the low-temperature (T $\sim$ 4 K) magneto-Raman scattering response of Bi_2Te_3/$FePS_3$ heterostructure with magnetic field in Faraday geometry, in the spectral region from 80 to 140 cm^{-1}. E_g^2 and A_{1g}^2 phonon modes of Bi_2Te_3 are designated as BT_1 and BT_2 respectively. Phonon modes (BT_1, BT_2) of both Bi_2Te_3 and $FePS_3$ (P2, P3, Magnon (M)) are visible in the colour map. The magnon mode at 120 cm^{-1} splits into two components M^* and M^- at/around 1 T. (b) Raman modes of $FePS_3$ with magnetic field in Voigt configuration at T$\sim$ 4K. The magnon mode splits at/around 16 T. (c) Raman modes of Bi_2Te_3/$FePS_3$ heterostructure with magnetic field in Voigt configuration at T $\sim$ 4 K. The magnon mode in $FePS_3$ splits at lower field ($\sim$ 9 T) compared to isolated $FePS_3$. (d) No magnetic field dependence was observed in the phonon modes of Bi_2Te_3. (e) Magnon frequency was plotted with magnetic field for both isolated $FePS_3$ and Bi_2Te_3/$FePS_3$ heterostructures in Voigt geometry. The magnon splitting occurs much lower field ($\sim$ 9 T) in heterostructure compared to splitting field in isolated $FePS_3$ ($\sim$ 16 T) (f) Optical microscopy image of Bi_2Te_3/$FePS_3$ heterostructure. High magnetic field Raman spectroscopy was performed in this heterostructure. The area marked with dotted red circle indicates the heterostructure region.

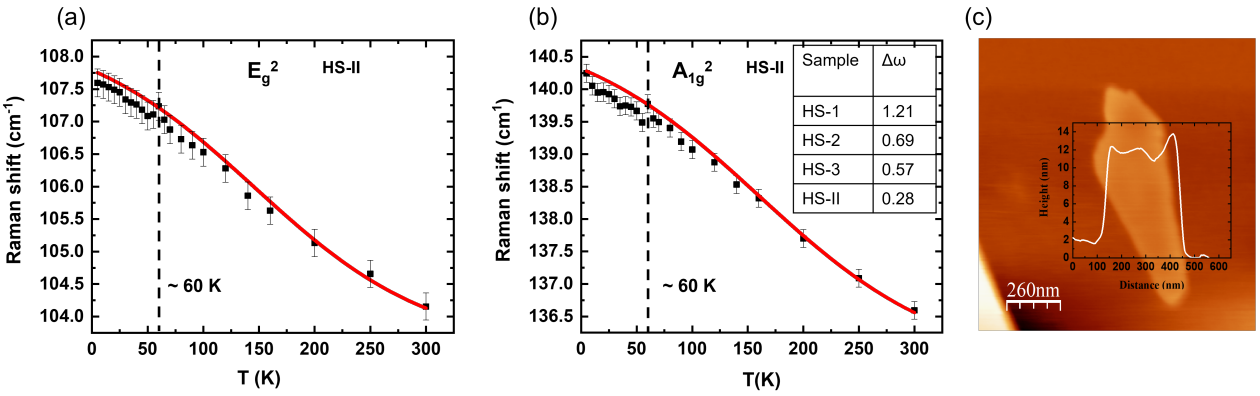

FIG. S25. Temperature dependent Raman modes of Bi_2Te_3 in HS-II. (a) In-plane (E_g^2) phonon mode; (b) out-of-plane (A_{1g}^2) phonon mode. Insets of figure (b) shows the reduction of $\Delta\omega$ with heterostructure thickness. HS (1-3) was already mentioned in the manuscript. HS-II is freshly prepared heterostructure. (c) Atomic force microscopy (AFM) image of thinner Bi_2Te_3 used in fabricating new heterostructures (HS-I, HS-II). The thickness of the flake is $\sim$ 12 nm confirmed by the height profile.

Bi_2Te_3		
Raman Modes	$\omega(cm^{-1})$(Expt)	$\omega(cm^{-1})$(Theory)
E_g	-	36
A_{1g}	-	54
E_g	**106**	**104**
A_{1g}	**138**	**138**

TABLE I. Irreducible representations of the Raman-active modes of bulk Bi_2Te_3. Only the high frequency E_g and A_{1g} modes are observed in experiments (second column).

$FePS_3$			
Raman Modes	$\omega(cm^{-1})$(zigzag)	$\omega(cm^{-1})$(FM)	$\Delta_\lambda^{rel}(\%)$
B_g	97	95	-2.46
A_g	**115**	**102**	-11.56
A_g	**141**	**137**	-2.97
B_g	140	146	3.71
B_g	203	205	0.74
A_g	208	211	1.73
B_g	214	214	0.09
A_g	225	230	2.31
B_g	256	259	0.90
A_g	268	268	0.04
A_g	356	359	0.84
A_g	536	538	0.32
B_g	529	529	0.04
A_g	546	547	0.18

TABLE II. Irreducible representations of the Raman-active modes of $FePS_3$. Phonon frequencies are calculated for zig-zag AFM (z-AFM) and FM spin configurations. Relative angular frequency shift ($\Delta_\lambda^{rel} = \frac{\omega_{FM}-\omega_{z-AFM}}{\omega_{z-AFM}} \times 100\%$) due to change in the magnetic ordering of the Raman-active modes is given in the last column.

Type of samples/ heterostructure	Experimental Techniques	Remarks
Cr-doped $(Bi,Sb)_2Te_3$ (BST) film	Quantum transport measurements [Quantum anomalous Hall effect (QAHE)]	Magnetic doping introduces detrimental effects leading to a very low operational temperature 30K (**Science 2013, 340, 167.)**
V-doped BST film	Quantum transport measurements (QAHE)	Operational temperature was slightly increasing that was at around 120 mK (**Nat. Mater. 2015, 14, 473**)
Modulation-doped [Cr:BST/BST] pentalayer heterostructure	Quantum transport measurements (QAHE)	There was slight improvement of the zero field QAHE temperature (2K) (**Nat. Mater. 2015, 14, 473; Appl. Phys. Lett. 2015, 107, 182401.)**
Proximity coupled BST films/TIG	Transport Measurement (AHE)	AHE observed at 400 K **(Sci. Adv. 2017, 3, e1700307.)**
Co-doped (Cr,V):BST film	Quantum transport measurements (QAHE)	QAHE temperature 1.5 K. (**Adv. Mater. 2018, 30, 1703062.)**
Proximity-coupled (Zn, Cr) Te/BST/(Zn,Cr)Te heterostructures	Quantum transport measurements (QAHE)	QAHE temperature 1.5 K. **(Appl. Phys. Lett. 2019, 115, 102403.)**
$MnBi_2Te_4/Bi_2Te_3$ superlattices	Quantum transport measurements (QAHE)	QAHE temperature 7 K. **(Nat. Phys. 2021, 17, 36.)**
$Bi_2Se_3/Y_3Fe_5O_{12}$	Magneto-optic Kerr effect (MOKE)	Indicate domain wall of flipping spins **(Nano Lett. 2014, 14, 3459.)**
EuS/Bi_2Se_3	Magnetic second-harmonic generation	Investigation of in-plane and out-of-plane ferromagnetic moments **(Nat. Commun. 2016, 7, 12014.)**
EuS/Bi_2Se_3 and EuS/BST	X-ray Magnetic Circular Dichroism	Challenges the claims of **Nat. Commun. 2016, 7, 12014 (Phys. Rev. Lett. 2020, 125, 226801.)**
EuS/Bi_2Se_3	PNR measurements	Magnetic moments are canted at the interface (**Nature 2016, 533, 513.)**
$Bi_2Te_3/FePS_3$	Raman spectroscopy	Proximity induced Spin phonon coupling in Bi_2Te_3; Reduction of Néel Temperature **(Current study)**

TABLE III. Performance comparisons of different Topological Insulator heterostructures using various experimental techniques

Modes	ω (cm^{-1}) (Bulk)	ω (cm^{-1}) (Monolayer)
E_g	36	36
A_{1g}	54	53
E_g	104	104
A_{1g}	138	142

TABLE IV. Irreducible representations of the Raman-active modes of bulk and single layer Bi_2Te_3.

System	E_1^{AFM} (Fig S7a) (eV)	E_2^{FM} (Fig S7b) (eV)	$J_{AFM} = \frac{(E_2^{FM} - E_1^{AFM})}{4S^2}$ (meV)	T_N (K)
$FePS_3$ Monolayer (expt.)	-102.180	-102.029	9.44	110
$FePS_3$ Monolayer (-0.5 % strain)	-103.834	-103.724	6.88	80
$Bi_2Te_3/FePS_3$ Heterostructure	-174.935	-174.839	5.96	69

TABLE V. Calculation of AFM exchange in $FePS_3$ monolayer with and without strain, and within the heterostructure setup involving Bi_2Te_3.

Thickness of $FePS_3$	Raman Mode (Peak position in cm^{-1})			Remarks
	SP1	SP2	SP3	No significant Raman shift was observed with thickness of $FePS_3$ from bulk to few layer
8 nm	247.08	279.17	380.19	
20 nm	247.56	279.23	380.08	
45 nm	247.72	279.40	380.16	
65 nm	247.53	279.13	380.01	
Bulk	247.86	279.47	380.23	

TABLE VI. The frequencies of $FePS_3$ spin-phonon (SP) coupled modes are presented with varying thickness (Figure S23). No significant Raman shift was observed with the thickness of $FePS_3$.

	Thickness	Raman Mode of Bi_2Te_3 (Peak position in cm^{-1})		Reference	Remarks
Bi_2Te_3 (Ar^+ laser)		E_g^2	A_{1g}^2	Nano Research 2013, 6(9): 688–692	❑ In-plane Raman mode (E_g^2) barely shows frequency shift with the thickness. ❑ Out-of-plane Raman mode (A_{1g}^2) exhibits a frequency shift ~ (6-7) cm^{-1} when reducing the thickness.
	1 QL	102	141		
	2 QL	102	135		
	7 QL	102	134		
	40 QL	102	135		
	Bulk	102.3	134		
Bi_2Te_3 Thin film (488 nm)	10 nm	101.4	132.9	J. Appl. Phys. 111, 054305 (2012)	
	50 nm	101.5	132.39		
Bi_2Te_3 Nanostructure (633 nm)	12 QL (Nanosheet)	98	140	Applied Surface Science 457(2018) 41-48	❑ Phonon modes of Bi_2Te_3 changes depending on the structure whether it is nanosheets or nanoplatelets.
	12 QL (Nanoplatelets)	99	127		
Bi_2Te_3 crystal and film (488 nm)	4 nm	101.4	132.9	Appl. Phys. Lett. 96, 153103 (2010)	❑ In-plane Raman mode (E_g^2) does not show significant frequency shift with the thickness. ❑ Out-of-plane Raman mode (A_{1g}^2) exhibits a frequency shift when reducing the thickness.
	40 nm	101.3	133.0		
	Bulk	101.7	134.0		
Bi_2Te_3	Bulk	104.0	138.0	Our work (Theory)	❑ Out-of-plane vibration mode shows frequency shift (~ 4 cm^{-1}) with thickness whereas in-plane phonon mode remains almost unchanged in frequency from bulk to monolayer. ❑ Phonon frequencies and the point group symmetry (D3d) remain invariant, irrespective of thickness.
	Monolayer	104.0	142.0		

TABLE VII. Thickness dependent Raman shift of Bi_2Te_3 with different structural form and wavelength excitation. No significant Raman shift was observed in E_g^2 mode and a prominent shift (~ 6 cm^{-1}) was observed in A_{1g}^2 mode with thickness.

Laser excitation (nm)	Thickness	Phonon dynamics (Peak Position)	Reference	Remarks
647.1	Dropcasted Bi_2Te_3 Nanoflakes (~15 nm)	Anharmonic in the temperature window (3 K to 295 K)	Sören Buchenau *et al*., Phys. Rev. B 101, 245431 (2020)	Bi_2Te_3 shows no phonon anomaly in frequency in the whole temperature window. It's a pure phonon-phonon coupling phenomena irrespective of thickness and laser wavelength excitation.
532	Bi_2Te_3 Single crystal (~ 135 μm)	Anharmonic in the temperature window (93K-298K)	Priyanath Mal *et al*. Phys. Chem. Chem. Phys., 2019, 21, 15030	
632	Mechanically exfoliated Bi_2Te_3 (20 nm & 60 nm)	Anharmonic in the temperature window (153 K to 303 K)	Manavendra P. Singh *et al*., Current Chinese Science, 2021, 1, 453-459	
533	Bi_2Te_3 Bulk film (~ 4 μm)	Linearly vary with temperature in the high temperature window (243 K to 573 K)	Duanhui Li *et al*., Phys. Status Solidi RRL 6, No. 6, 268–270 (2012)	Bi_2Te_3 shows no phonon anomaly in frequency and varies linearly in the high temperature window. (phonon-phonon coupling)
633	Bi_2Te_3 Nanowire and nanoribbon	Linearly vary with temperature in the high temperature window (243 K to 573 K)	Dambi Park *et al*., Scientific Reports 6, 19132 (2016)	
473	Exfoliated bulk Bi_2Te_3 flake (~ 140 nm, ~ 250 nm,> 500 nm)	Anharmonic in the temperature window (5 K-300 K)	Our work	1. Bi_2Te_3 (named as 'Isolated Bi_2Te_3' in the manuscript) shows no phonon anomaly in frequency in the whole temperature window. 2. Bi_2Te_3 shows phonon anomaly in frequency (spin-phonon coupling) at/ around 60 K due to $FePS_3$. Strength of spin-phonon coupling ($\Delta\omega$) reduces with thickness of individual material in the Bi_2Te_3/ $FePS_3$ heterostructure without affecting the characteristic temperature for spin-phonon coupling (~ 60K). 3. Bi_2Te_3 recover the anharmonicity when a hexagonal boron nitride (independent of thickness) is placed in between bulk Bi_2Te_3 and bulk $FePS_3$.
	Bulk Bi_2Te_3 (>500 nm)/ Bulk $FePS_3$ (~ 150 nm)	Deviation from anharmonicity at/around 60 K in Bi_2Te_3 (Spin-phonon coupling)		
	Bulk Bi_2Te_3 (~ 250 nm)/ Bulk $FePS_3$ (~ 88 nm)	Deviation from anharmonicity at/around 60 K in Bi_2Te_3 (Spin-phonon coupling) Strength of coupling reduces.		
	Bulk Bi_2Te_3 (~ 140 nm)/ Bulk $FePS_3$ (~ 10 nm)	Deviation from anharmonicity at/around 60 K in Bi_2Te_3 (Spin-phonon coupling). More reduction of strength of spin-phonon coupling.		
	Bulk Bi_2Te_3 (>500 nm) /Bulk hBN (>100 nm)/Bulk $FePS_3$ (~ 150 nm)	Anharmonic in the temperature window (5 K-300K).		
	Bulk Bi_2Te_3 (>500 nm) /few layer hBN (~ 10 nm)/Bulk $FePS_3$ (~ 150 nm)	Anharmonic in the temperature window (5 K-300K).		

TABLE VIII. Phonon dynamics of Bi_2Te_3 with temperature for a fixed thickness of Bi_2Te_3. Bi_2Te_3 shows no phonon anomaly in frequency with temperature irrespective of thickness, wavelength excitation and different form of Bi_2Te_3. It is pure phonon-phonon coupling.

Structure	Configuration	Magnon splitting field (Tesla)
$FePS_3$	Faraday	1
	Voigt	16
BT	Faraday	No magnetic field dependency
	Voigt	No magnetic field dependency
BT/$FePS_3$ (Heterostructure)	Faraday	1
	Voigt	9

TABLE IX. Magnon splitting field in $FePS_3$, Bi_2Te_3 and $Bi_2Te_3/FePS_3$ heterostructures in different magnetic field configurations.